Multi-view light-sheet imaging and tracking with the MaMuT software reveals the cell lineage of a direct developing arthropod limb

Carsten Wolff[1, *, †], Jean-Yves Tinevez[2, *], Tobias Pietzsch[3, *], Evangelia Stamataki[4], Benjamin Harich[3, ¶], Leo Guignard[4], Stephan Preibisch[5], Spencer Shorte[2], Philipp J. Keller[4], Pavel Tomancak[3, †], and Anastasios Pavlopoulos[4, †, §]

[1] Institut für Biologie, Humboldt-Universität zu Berlin, 10115 Berlin, Germany.
[2] Imagopole, Citech, Institut Pasteur, 75015 Paris, France.
[3] Max Planck Institute of Molecular Cell Biology and Genetics, 01307 Dresden, Germany.
[4] Janelia Research Campus, Howard Hughes Medical Institute, Ashburn, Virginia 20147, USA.
[5] Berlin Institute for Medical Systems Biology, Max Delbrück Center for Molecular Medicine, D-13125 Berlin, Germany.

[¶] Present address: Radboud University Medical Center, Donders Institute for Brain Cognition and Behaviour, Department of Human Genetics, Nijmegen 6525 GA, The Netherlands.

[*] Co-first authors

[†] Corresponding authors carsten.wolff@web.de
tomancak@mpi-cbg.de
pavlopoulosa@janelia.hhmi.org

[§] Lead Contact Anastasios Pavlopoulos
+1-571-209-4000 (ex. 3337)
pavlopoulosa@janelia.hhmi.org

Abstract

During development, coordinated cell behaviors orchestrate tissue and organ morphogenesis. Detailed descriptions of cell lineages and behaviors provide a powerful framework to elucidate the mechanisms of morphogenesis. To study the cellular basis of limb development, we imaged transgenic fluorescently-labeled embryos from the crustacean *Parhyale hawaiensis* with multi-view light-sheet microscopy at high spatiotemporal resolution over several days of embryogenesis. The cell lineage of outgrowing thoracic limbs was reconstructed at single-cell resolution with new software called Massive Multi-view Tracker (MaMuT). *In silico* clonal analyses suggested that the early limb primordium becomes subdivided into anterior-posterior and dorsal-ventral compartments whose boundaries intersect at the distal tip of the growing limb. Limb-bud formation is associated with spatial modulation of cell proliferation, while limb elongation is also driven by preferential orientation of cell divisions along the proximal-distal growth axis. Cellular reconstructions were predictive of the expression patterns of limb development genes including the BMP morphogen Decapentaplegic.

Introduction

Morphogenesis, or the origin of biological form, is one of the oldest and most enduring problems in biology. Embryonic tissues change their size and shape during development through patterned cell activities controlled by intricate physico-chemical mechanisms (Day and Lawrence, 2000; Heisenberg and Bellaiche, 2013; Keller, 2013; Keller, 2012; Lecuit and Mahadevan, 2017; LeGoff and Lecuit, 2015). Developmental processes have been explained traditionally in terms of genes and gene regulatory networks, and a major challenge is to understand how the genetic and molecular information is ultimately translated into cellular activities like proliferation, death, change of shape and movement. Therefore, detailed descriptions of cell lineages and behaviors can provide a firm ground for studying morphogenesis from a bottom-up cellular perspective (Buckingham and Meilhac, 2011; Kretzschmar and Watt, 2012; Schnabel et al., 1997; Spanjaard and Junker, 2017; Sulston et al., 1983).

We have focused here on the crustacean *Parhyale hawaiensis* that satisfies a number of appealing biological and technical requirements for multi-level studies of appendage (limb) morphogenesis (Stamataki and Pavlopoulos, 2016). *Parhyale* is a direct developer; its body plan is specified during the 10 days of embryogenesis when imaging is readily possible (Browne et al., 2005). Each embryo develops a variety of specialized appendages along the anterior-posterior axis that differ in size, shape and pattern (Martin et al., 2016; Pavlopoulos et al., 2009; Wolff and Scholtz, 2008). *Parhyale* eggs have good size and optical properties for microscopic live imaging at cellular resolution; the eggshell is transparent and embryos are 500 μm long with low autofluorescence and light scattering. Several functional genetic approaches, embryological treatments and genomic resources also allow diverse experimental manipulations in *Parhyale* (Kao et al., 2016).

Previous reports have used transmitted light and fluorescence time-lapse microscopy to live image early processes like gastrulation and germband formation during the first couple days of *Parhyale* development (Alwes et al., 2011; Chaw and Patel, 2012; Hannibal et al., 2012). However, for a comprehensive coverage of *Parhyale* limb formation, embryos need to be imaged from multiple angular viewpoints from day 3 to

day 8 of embryogenesis (Browne et al., 2005). We demonstrate here that transgenic embryos with fluorescently labeled nuclei can be imaged routinely for several consecutive days using Light-sheet Fluorescence Microscopy (LSFM). LSFM is an ideal technology for studying how cells form tissues and organs in intact developing embryos (Huisken et al., 2004; Keller et al., 2008; Truong et al., 2011). It enables biologists to capture fast and dynamic processes at very high spatiotemporal resolution, over long periods of time, and with minimal bleaching and photo-damage (Combs and Shroff, 2017; Huisken and Stainier, 2009; Khairy and Keller, 2011; Schmied et al., 2014; Weber et al., 2014). In addition, samples can be optically sectioned from multiple angles (multi-view LSFM) that can be combined computationally to reconstruct the entire specimen with more isotropic resolution (Chhetri et al., 2015; Krzic et al., 2012; Schmid et al., 2013; Swoger et al., 2007; Tomer et al., 2012; Wu et al., 2016; Wu et al., 2013).

Although the amount and type of data generated by multi-view LSFM raise several challenges for image analysis, many of them have been efficiently addressed. Software solutions exist for registration of acquired views, fusion of raw views (z-stacks) into a single output z-stack, and visualization of the raw and fused images (Chhetri et al., 2015; Ingaramo et al., 2014; Pietzsch et al., 2015; Preibisch et al., 2014; Preibisch et al., 2010; Rubio-Guivernau et al., 2012; Wu et al., 2016). These processes should be repeated for hundreds or thousands of time-points to generate a 4D representation of the embryo as it develops over time (Amat et al., 2015; Schmied et al., 2014; Schmied et al., 2016). Automated approaches for cell segmentation and tracking have also been developed (Amat et al., 2014; Du et al., 2014; Dufour et al., 2017; Faure et al., 2016; Schiegg et al., 2015; Stegmaier et al., 2016; Ulman et al., 2017), however they do not yet reach the precision required for unsupervised extraction of cell lineages. To address this issue, we describe here the Massive Multi-view Tracker (MaMuT) software that allows visualization, annotation, and accurate lineage reconstruction of large multi-dimensional microscopy data.

We quantitatively analyzed *Parhyale* LSFM datasets with MaMuT to understand the cellular basis of arthropod limb morphogenesis. As revealed by lineage tracing

experiments in the leading arthropod model *Drosophila melanogaster*, the leg and wing primordia become progressively subdivided into distinct cell populations (called compartments when lineage-restricted) along the anterior-posterior (AP) and dorsal-ventral (DV) axes (Dahmann et al., 2011; Garcia-Bellido et al., 1973; Steiner, 1976). Tissue subdivisions acquire distinct cell fates driven by domain-specific expression of patterning genes (called selectors if lineally inherited), as well as by the localized induction of signaling molecules at compartment boundaries (organizers) that control patterning and growth of developing organs (Garcia-Bellido, 1975; Lawrence and Struhl, 1996; Mann and Carroll, 2002; Restrepo et al., 2014).

Besides regionalization mechanisms, oriented cell divisions have been implicated as a general mechanism in shaping the *Drosophila* wing and other growing organs (Baena-Lopez et al., 2005; Legoff et al., 2013; Mao et al., 2013). Other mechanisms like differential cell proliferation and cell rearrangement could also play a role in the formation of limb buds and their elongation along the proximal-distal (PD) axis. So far, these processes have not been possible to live image and quantify in direct developing arthropod limbs. Our understanding of cell dynamics shaping arthropod limbs has relied exclusively on studies of the indirectly developing *Drosophila* limbs (primarily the wing disc) using clonal analysis and lineage tracing across fixed specimens (Baena-Lopez et al., 2005; Gonzalez-Gaitan et al., 1994; Resino et al., 2002; Weigmann and Cohen, 1999; Worley et al., 2013) and recent improvements in imaging discs *in vivo* and *ex vivo* (Dye et al., 2017; Heemskerk et al., 2014; Legoff et al., 2013; Mao et al., 2013; Strassburger et al., 2017; Tsao et al., 2016; Zartman et al., 2013).

By tracking all constituent cells in direct developing *Parhyale* limbs, we identified the lineage restrictions and morphogenetic cellular behaviors operating during limb bud formation and elongation, and compared these to *Drosophila* and other arthropod and vertebrate paradigms. We validated our cellular models of morphogenesis by studying the expression of developmental regulatory genes implicated in limb patterning and growth.

Results

Imaging *Parhyale* embryogenesis with multi-view LSFM

Three-day old transgenic embryos with fluorescently labeled nuclei were mounted for LSFM in low melting agarose with scattered fluorescent beads. Several parameters were optimized to cover all stages of *Parhyale* appendage development at single-cell resolution with adequate temporal sampling for accurate cell tracking (see Materials and methods). A typical 4 to 5-day long recording was composed of more than 1 million images resulting in >7 TB datasets.

The relatively slow tempo of *Parhyale* development enabled imaging of each embryo from multiple highly overlapping views with minimal displacement of nuclei between views acquired in each time-point (Figure 1A). As detailed in Materials and methods, development of the entire embryo was reconstructed using the Fiji (Fiji Is Just ImageJ) biological image analysis platform (Schindelin et al., 2012) according to the following steps: 1) image file preprocessing, 2) bead-based spatial registration of views in each time-point, 3) fusion by multi-view deconvolution, 4) bead-based temporal registration across time-points, 5) computation of temporally registered fused volumes, and 6) 4D rendering of the spatiotemporally registered fused data (Preibisch et al., 2014; Preibisch et al., 2010; Schmied et al., 2014). This processing resulted in almost isotropic resolution of fused volumes (Figure 1B) and was used for visualization of *Parhyale* embryogenesis with cellular resolution (Figure 1C–K and Figure 1—video 1).

Segment formation and maturation in *Parhyale* occurred sequentially in AP progression (Figure 1—video 2). Appendage morphogenesis involved patterning, growth and differentiation of ectodermal cells organized in an epithelial monolayer that gave rise to the appendage epidermis. In our LSFM recordings, we were particularly interested in imaging the limbs in the anterior thorax of *Parhyale* embryos that were specified at about 3.5 days after egg-lay (AEL) at 25˚C. Over the next 4 days, limb buds bulged out ventrally, elongated along their PD axis and became progressively segmented until they acquired their definite morphology at around 8 days AEL (Figure 1C–K and Figure 1—video 2).

During germband formation, the ectoderm contributing to the posterior head and the trunk became organized in a stereotyped grid-like pattern with ordered AP rows and DV columns of cells (Figure 2A–A'') (Browne et al., 2005; Dohle et al., 2004; Dohle and Scholtz, 1988; Gerberding et al., 2002; Scholtz, 1990; Wolff and Gerberding, 2015). Each row of cells corresponded to one parasegment, which is the unit of early metameric organization in *Parhyale* embryos, like in *Drosophila* and other arthropods (Hejnol and Scholtz, 2004; Scholtz et al., 1994). Two rounds of longitudinally-oriented cell divisions in each formed parasegmental row (Figure 2B–D'), together with the progressive addition of new parasegments at the posterior end, led to embryo axial elongation (Figure 1C–H). Subsequent divisions of ectodermal cells had a more complex pattern disrupting the regularity of the grid and contributing to the transition from parasegmental to segmental body organization and the evagination of paired appendages in each segment. Appendage buds appeared successively from the head region backwards (Figure 1D–H) and started lengthening (Figure 1F–K) and differentiating along their PD axis (Figure 1G–K). At the end of the imaging period, morphogenesis appeared nearly complete. Thus, multi-view LSFM imaging captured the entire gamut of differential appendage morphogenetic events along the body axis of the *Parhyale* embryo in a single time-lapse experiment.

MaMuT: a platform for cell tracking in multi-view and multi-terabyte datasets

To examine the cellular basis of morphogenesis, we developed a novel Fiji plugin to extract cell lineages from multi-view and multi-terabyte datasets. This tool was dubbed MaMuT for Massive Multi-view Tracker (Figure 3) and is a hybrid and extension of two existing Fiji plugins: the BigDataViewer visualization engine (Pietzsch et al., 2015) and the TrackMate annotation engine (Tinevez et al., 2016). MaMuT can be installed through the Fiji updater and is tightly integrated with the other Fiji plugins for LSFM data processing. The source code for MaMuT is available on GitHub (Tinevez et al., 2018) and detailed tutorials and training datasets can be found at http://imagej.net/MaMuT.

MaMuT is an interactive, user-friendly tool for visualization, annotation, tracking and lineage reconstruction of large multi-dimensional microscopy data (Figure 3 and Figure 3—figure supplement 1). It is a versatile platform that can be used either for manual or

semi-automated tracking of selected populations of cells of interest, or for visualization and editing of fully automated computational predictions for systems-wide lineage reconstructions. MaMuT can handle multiple data sources but was developed primarily to enable the analysis of LSFM datasets. Its unique feature is the ability to annotate image volumes synergistically from all available input views (detailed in Materials and methods). This functionality of MaMuT allowed us to identify and track all constituent cells in developing limbs continuously from the early germband stages until the later stages of 3D organ outgrowth, when the information from multiple views was required for full reconstructions.

Single-cell lineage reconstruction of a *Parhyale* thoracic limb

We deployed the manual version of MaMuT to extract the lineage of one *Parhyale* thoracic limb. By convention, *Parhyale* parasegments are identified by ascending indices E1, E2, E3 etc., the AP rows of ectodermal cells in each parasegment by the letters a, b, c and d, and the DV columns of cells in each parasegment by numbers (Figure 2). In accordance with previous studies in malacostracan crustaceans and other arthropods, our reconstructions demonstrated that each *Parhyale* thoracic limb consisted of cells from two neighboring parasegments (Browne et al., 2005; Dohle et al., 2004; Dohle and Scholtz, 1988; Hejnol and Scholtz, 2004; Scholtz, 1990; Scholtz et al., 1994; Wolff and Scholtz, 2008). The T2 limb (referred to as limb#1) that we analyzed in-depth (Figure 4A–E) developed from rows b, c and d of the E4 parasegment and from rows a and b of the following E5 parasegment (Figure 4F–J'). Cells that arose from rows c, d and a occupied the entire length of the limb and body wall parts of the T2 segment, while rows b contributed only to the proximal limb and intersegmental territories (Figure 4—figure supplement 1K–O'). Cells in medial columns 1 and 2 gave rise to the nervous system and sternites and were not considered in this study. The more lateral columns 3 to 9 gave rise to the forming limb (Figure 4—figure supplement 1F–J).

We fully tracked 34 founder cells constituting the limb#1 primordium over 50 hours of development, giving rise to a total of 361 epidermal cells (Figure 5 and Figure 5—video 1). We started tracking each of these 34 cells as they divided longitudinally from the 2-

row to the 4-row-parasegment (Figure 5A–C), and then continuously during the subsequent rounds of divisions, referred to as differential divisions (DDs) (Figure 5D). The number of DDs observed during these 50 hours varied dramatically between cells from just 1 DD in the slowest dividing lateral cells of the primordium (cells E4b8, E5a9/b9) to 5 DDs in the fastest dividing central cells (cells E4c3-c6 and E4d3-d6). Although the clonal composition of crustacean appendages had been described previously with lipophilic dye injections (Wolff and Scholtz, 2008), the reconstruction presented here is the most comprehensive lineage tree for any developing arthropod limb published to date (Figure 5—figure supplement 1).

Early lineage restrictions along the AP and DV axes

We first asked whether these complete reconstructions could reveal any lineage-based subdivisions in the developing limb#1. The AP restriction at the border of neighboring parasegments at the 1-row stage has been revealed in *Parhyale* and other embryos by embryological descriptions, lineage tracing and expression studies for the *engrailed* (*en*) gene that marks the posterior compartment (Browne et al., 2005; Dohle et al., 2004; Dohle and Scholtz, 1988; Hejnol and Scholtz, 2004; Patel et al., 1989; Scholtz, 1990; Scholtz et al., 1994). In agreement with this AP restriction, during limb specification and outgrowth there was a straight clonal boundary running between the anterior cells derived from the E4b, c and d rows and the posterior cells derived from the E5a and b rows (Figure 4F–J' and Figure 4—figure supplement 1K–O').

After the well-known AP boundary, we sought to identify any subdivision along the DV axis. Compartments were classically discovered by clonal analysis using mitotic recombination. In our reconstructions, we could generate clones digitally from arbitrary cells at different stages of development. We reasoned that we could reveal the timing and position of any heritable DV restriction by piecing together correctly all founder cells of dorsal or ventral identity in a way that the two polyclones (i.e. compartments) would stay separate and form a lasting straight interface between them. This analysis suggested that there is indeed a DV separation that took place at the 4-row-parasegment. The DV boundary ran between the E4b and c rows anteriorly, between the E5a and b rows

posteriorly, and between cells E4c4-c5, E4d3-d4 and E5a4-a5 medially (Figure 4F). Throughout limb#1 development, the dorsal and ventral cells formed a sharp boundary between themselves extending along the PD axis (Figure 4F–J').

To investigate the stereotypy of the AP and DV separation across *Parhyale* limbs, we analyzed a second, independently imaged and reconstructed T2 limb (referred to as limb#2) from a different embryo (Figure 4—figure supplement 2A–D). Four identical compartments (anterior-dorsal, anterior-ventral, posterior-dorsal and posterior-ventral) could be derived in this independent reconstruction with straight boundaries and no cell mixing between neighboring compartments (Figure 4—figure supplement 2E–H'). These results suggested that *in silico* studies of comprehensive and accurate lineages can provide novel insights into clonal subdivisions in species where sophisticated genetic methodologies for lineage tracing are not implemented yet.

Cellular dynamics underlying limb morphogenesis

The first T2 limb (limb#1) was lineaged with the new MaMuT software from a multi-view acquisition of an embryo imaged at 26˚C (Figure 4), while the second T2 limb (limb#2) was lineaged with the previously developed SIMI°BioCell software (Hejnol and Scholtz, 2004; Schnabel et al., 1997) from a single-view of another embryo imaged at 29-30˚C (Figure 4—figure supplement 2). Analysis of the birth sequence of the founder cells in the two reconstructed T2 limbs largely confirmed that the second mitotic wave creating the 4-row-parasegment propagated from anterior to posterior rows and from medial to lateral columns (Figure 5A–C and Figure 5—source data 1). For example, division of the ab cells in parasegment E4 had already progressed to column 5 or even more laterally before ab3 divided in the next posterior parasegment E5. However, we also found two notable deviations from this general pattern. First, as previously noted (Scholtz, 1990), division of the posterior cd cells within the 2-row-parasegment was slightly more advanced temporally compared to their anterior ab sister cells (Figure 5A–C). Second, the temporal sequence of divisions, which gave rise to a stereotyped number and spatial arrangement of the 34 founder cells in each primordium, exhibited a certain degree of variability between the two analyzed limbs; for example, division of the

E4cd8/9 cells preceded division of E4cd7 in limb#1 but not in lim#2, whereas division of the E4cd6/7 cells preceded division of E4cd5 in limb#2 but not in limb#1 (Figure 5A–B).

We then examined the increase in cell number over time in the two limbs during the analyzed stages of limb outgrowth. The embryo with limb#2 imaged at higher temperature exhibited a faster growth rate compared to the embryo with limb#1 (Figure 5D). Yet, it was possible to register the two growth curves during the period when all cells were tracked faithfully by applying a linear temporal rescaling factor of 1.6, effectively correcting for the temperature-induced change in growth (Figure 5D). After this temporal alignment, the increase in cell number was very similar between developing limbs, up to 35 hours after the first tracked division. The matching curves demonstrated that cell numbers were highly reproducible between developing limbs after aligning them temporally and allowed their pairwise quantitative comparison (see next section). Beyond this time-point, it was not possible to track all cells in the outgrowing limb#2 due to their increasing higher density, the deterioration of the fluorescence signal along the detection axis and the lack of the multi-view information for lineaging this limb.

Limb bud formation entailed the remodeling of the flat epithelium into a 3D bulge (Figure 4A–C and Figure 4—figure supplement 2A–C). At the cellular level, the first step in this transformation was the rise of few cells at the intersection of the four compartments above the level of the germband at around 96 hours AEL (Figure 4G,G' and Figure 4—figure supplement 2F,F'). Within the following 3 hours, this initial phase was followed by a large-scale elevation of most cells in the dorsal compartment. As this elevation continued, the medial ventral cells folded and became apposed to the medial dorsal cells forming the convex surface of the limb bud (Figure 4H,H' and Figure 4—figure supplement 2G,G'). The intersection of the AP and DV boundaries was at the tip of the limb bud and persisted in this position throughout subsequent elongation (Figure 4H–J' and Figure 4—figure supplement 2G–H'). From 103 hours AEL onwards, a second element appeared bulging distally off the original bud in limb#1 (Figure 4I,I'). The limb elongated as a convoluted rather than straight cylinder and acquired progressively an S-shape (Figure 4J,J').

Quantification of differential cell behaviors during limb bud formation and elongation

Two cell behaviors implicated in organ morphogenesis were readily quantifiable in our nuclear trackings: the pattern of cell proliferation and the orientation of cell divisions. These cell activities have been traditionally inferred from the distribution, size and shape of somatic clones induced in developing tissues (Baena-Lopez et al., 2005; Gonzalez-Gaitan et al., 1994; Mao et al., 2013; Resino et al., 2002; Weigmann and Cohen, 1999; Worley et al., 2013). This approach could be also adapted here by generating *in silico* clones (Figure 6—figure supplement 1). Yet, the MaMuT reconstructions enabled us to enrich the lineage information with rigorous quantitative analyses of the rate and orientation of mitotic divisions for all tracked nuclei.

First, we calculated the cell cycle length (CCL), i.e. the branch length for every constituent cell in the lineage of limb#1 (Figure 6A–D and Figure 6—figure supplement 2). This quantification revealed a striking difference in CCL between central cells that were dividing faster than their neighbors in the periphery of the primordium (average CCL 7.1-8.5 hours versus 8.5-16.4 hours, respectively). This difference started from early primordium specification at the 4-row-parasegment (Figure 6E), but became most pronounced during the global elevation of the limb bud (Figure 4F), suggesting a causal association between spatially controlled cell proliferation and initiation of limb outgrowth (see Discussion). During subsequent elongation stages, a high concentration of fast dividing cells was located at the intersection of the four presumptive compartments, resembling a growth zone at the distal tip of the growing appendage (Figure 6G,H). Another row of faster dividing cells was localized in the anterior cells abutting the AP boundary (Figure 6H,H').

To explore the levels of variability in the pattern of cell divisions, we performed a hierarchical clustering of the founder cells within each of the two analyzed T2 limbs based on a lineage distance metric computed from the division patterns exhibited by the 34 cells (see Material and methods). This analysis revealed very similar profiles in the

two limbs, as well as their average, with their cells forming three clusters (Figure 7A–C and Figure 7—source data 1): the first cluster contained cells E4c3-c7 and E4d3-d7 displaying the fastest proliferation rates and giving rise to most of the limb structures; the second cluster contained the majority of E4 and E5 b cells corresponding to the slowest dividing cells of ventral fate and contributing to the proximal limb and intersegmental territories; the third cluster contained the remaining cells exhibiting mixed division patterns, including most of the posterior E5a cells and the more lateral E4c and d cells. This clustering suggested that a common set of patterning mechanisms operates across T2 limbs specifying the distinct properties of these groups of cells. At the same time, the linkages and distances of cells within each cluster varied from identical (e.g. E4b3/b4) to very different (e.g. E4d4/d5) between limbs, revealing a certain degree of flexibility in the behaviors exhibited by homologous cells in a limb-specific manner. Extra support for this interpretation came from plotting the distribution of the lineage distances between founder cells across the two limbs. Pairwise comparisons revealed low distances between the 34 homologous cells in limb#1 and limb#2 with a median difference of 19.3% (Figure 7D). Thus, homologous cells exhibited similar but not identical division patterns across limbs. The distribution of these distances between homologous cells was significantly shifted towards lower values relative to pairwise comparisons between non-homologous cells across the two limbs (Figure 7D and Figure 7—source data 1).

Next, we looked for any biases in the orientation of mitotic divisions that could be associated with limb morphogenesis (Figure 8A–E). All early divisions in the limb#1 primordium were parallel to the AP axis confirming the strict longitudinal orientation of row divisions (Figure 8F). Cell divisions acquired a more heterogeneous pattern after the 4-row-parasegment (Figure 8G). An increasing number of mitotic spindles aligned progressively along the PD axis during limb bud formation (Figure 8H) and elongation (Figure 8I,J). Collectively, the information extracted from our spatiotemporally resolved lineage trees strongly suggested that *Parhyale* limb outgrowth is driven by at least two patterned cell behaviors: the differential rates of cell proliferation and the orderly arrangement of mitotic spindles.

Cellular basis of the elaboration of the limb PD axis

To understand the cellular basis of the establishment of positional values along the PD axis, we followed the fate of cells during T2 limb#1 segmentation. Segmentation involved the progressive subdivision of the elongating PD axis into an increasing number of elements (Figure 9A–L). We tracked neighboring cells in columns E4c (cells E4c5-c8, not shown) and E5a (cells E5a5-a8, shown in Figure 9A–F) from 84 to 151 hours AEL. These cells were ideal for reconstructing the PD axis at single-cell resolution because they mostly divided proximodistally forming elongated thin clones (Figure 6—figure supplement 1).

This analysis showed that the cells that gave rise to the proximal, medial and distal limb segments occupied distinct mediolateral positions in the germband grid at the 4-row-parasegment (Figure 9M) and distinct PD positions in the early limb bud (Figure 9N). When the limb bud split into two elements, the proximal element gave rise to the proximal limb segments coxa, basis and ischium, while the distal element gave rise to the distal limb segments merus, carpus, propodus, and dactylus (Figure 9O–R). The cells forming the distal segments originated as a disc of cells centered at the intersection of the 4 compartments with contributions from the E4c4-c6, E4d3-d6 and E5a3-a6 sublineages (Figure 9—figure supplement 1). During the subsequent elongation stages, distal cells kept separate from more proximal cells at the prospective ischium/merus joint, suggesting that limb segments may pose secondary lineage restrictions along the PD axis (Figure 9—figure supplement 1) (Milan and Cohen, 2000). This first ischium/merus subdivision (Figure 9O) was followed by the basis/ischium subdivision (Figure 9P), the propodus/dactylus, carpus/propodus and coxa/basis subdivisions (Figure 9Q), and the carpus/merus subdivision (Figure 9R).

Expression of limb patterning genes validates cellular models of *Parhyale* limb morphogenesis

To test our cellular models and make a first link between expression of limb patterning genes and morphogenetic cell behaviors, we analyzed by in situ hybridization the expression of the *Parhyale decapentaplegic* (*Ph-dpp*) gene that encodes a Bone

Morphogenetic Protein 2/4 signaling molecule (Figure 10—figure supplement 1G). In *Drosophila*, Dpp signaling controls dorsal cell fate in the leg and growth via cell proliferation in the wing (Barrio and Milan, 2017; Bosch et al., 2017; Brook and Cohen, 1996; Matsuda and Affolter, 2017; Rogulja and Irvine, 2005; Svendsen et al., 2015). Therefore, probing *Ph-dpp* expression in *Parhyale* limb buds could provide a direct test for our cell-based predictions regarding the DV lineage restriction and the differential cell proliferation rates in the limb primordium.

Analysis of embryos 84-96 hrs AEL revealed alternating regions of high/moderate and low/no *Ph-dpp* expression in the anterior thoracic region (Figure 10A,A'and Figure 10—figure supplement 1A,A'). We used MaMuT to annotate both the gene expression and identity of cells in stained T2 limbs at cellular resolution. Acknowledging that the graded *Ph-dpp* expression obscured the precise limits of its expression, this analysis suggested that the region of high/moderate *Ph-dpp* expression was localized to rows E4c, E4d and E5a that mostly contribute to the presumptive dorsal compartment, while low/no *Ph-dpp* expression could be detected in the prospective ventral rows E4b anteriorly and E5b posteriorly (Figure 10A''). Furthermore, *Ph-dpp* expression faded in the medial (prospective ventral) columns and the border between high/moderate and low/no expressing cells was located in descendent cells from column 4 as also predicted by our *in silico* cellular analysis (Figure 10A–A''). In embryos 96-108 hrs AEL, the domain of strong *Ph-dpp* expression was more localized in the row of anterior-dorsal cells abutting the AP boundary (Figure 10D–D'' and Figure 10—figure supplement 1D,D').

To get an insight into the downstream effects of Dpp signaling in the *Parhyale* limb, we also analyzed expression of the Tbx6/*Dorsocross* (*Doc*) gene (Figure 10—figure supplement 1H) that responds to high levels of Dpp signaling in the dorsal region of the *Drosophila* embryo and leg disc (Svendsen et al., 2015). Expression of the single *Doc* gene identified in *Parhyale* (*Ph-Doc*) was detected in a subset of the *Ph-dpp*-expressing cells at 84-96 hrs AEL (Figure 10B–B'' and Figure 10—figure supplement 1B,B'), while 12 hrs later the two genes exhibited essentially identical strong expression in the cells abutting the AP boundary (Figure 10E–E'' and Figure 10—figure supplement 1E,E'). In

both stages analyzed, cells expressing *Ph-dpp* and *Ph-Doc* also exhibited the highest rates of cell proliferation (compare Figure 10D'',E'' with Figure 6G,H) providing strong correlative evidence for a morphogen-dependent control of *Parhyale* limb growth.

As a last validation of our cellular models, we probed the expression of the *Parhyale H15* (*Ph-H15*) gene during early limb formation (Figure 10—figure supplement 1H). In *Drosophila* and other arthropods studied, the Tbx20 genes *H15*/*midline* act antagonistically to dorsal selector genes and control ventral cell fate in developing legs (Janssen et al., 2008; Svendsen et al., 2015). Our model for the timing and position of limb DV compartmentalization predicted that *Ph-H15* would come up in the b cells from the 4-row-parasegment stage onwards. In agreement with these predictions, in situ hybridization analyses detected the *Ph-H15* transcripts specifically in the b row cells. Furthermore, expression initiated shortly after the ab cells divided longitudinally into the a and b daughter cells in each forming 4-row-parasegment (Figure 10C–C'' and Figure 10—figure supplement 1C,C'). Although *Ph-H15* was first activated in all b cells, during later divisions *Ph-H15* expression faded in the more medial columns (Figure 10C–C'') and persisted only in the ventral limb cells close to the body wall (Figure 10F–F'' and Figure 10—figure supplement 1F,F').

All these results demonstrated how the reconstruction of cell lineages and behaviors can provide solid predictions and powerful contexts to study the expression and function of associated genes.

Discussion

We have established an integrated framework to study the cellular and genetic basis of developmental morphogenesis. By combining light-sheet microscopy with new software for cell tracking in large multi-dimensional datasets, we have revealed the cellular architecture and dynamics underlying epithelial remodeling and organ morphogenesis in a non-conventional experimental model.

Reconstruction of *Parhyale* embryogenesis with multi-view LSFM and MaMuT

The LSFM technology is empowering biologists to image developmental processes with unprecedented spatiotemporal resolution. Together with MaMuT-based lineaging and tracking, various experimental designs can be addressed ranging from analyzing a small subset of objects in the imaged volume to systems-wide analyses of all constituent parts.

The lineage reconstructions presented in this article were generated manually and required 2 to 3 months for each limb. More generally, manual lineaging efforts can take anything between few days to several months depending on the number of tracked cells, the complexity of the imaged tissue of interest, the duration of the tracked process, the quality of the image dataset, and the desired accuracy and completeness of the reconstructed lineages. The main advantage of manual tracking by experts is that the extracted lineage is more likely error-free compared to results of automated trackers that must be manually proofread before any meaningful analysis can be attempted. In addition to allowing reliable biological insights, manually generated lineages serve as important "ground truth" datasets for the application of machine learning based automated tracking solutions (Ulman et al., 2017).

Acknowledging that fully manual tracking is a laborious and repetitive task that may be impractical for large-scale comparative lineaging approaches, the latest MaMuT architecture offers, in addition to manual tracking, two functionalities for automated tracking: i) a semi-automated option where individual nuclei can be selected by the user and tracked computationally over time, and ii) the option to import into MaMuT fully automated annotations generated by the Tracking with Gaussian Mixture Models (TGMM) software (Amat et al., 2014), which is currently one of the most accurate and computationally efficient methods for segmentation and tracking of fluorescently labeled nuclei. After the import, MaMuT can be used to manually proofread and correct the results of the automated tracking pipeline. However, we also note that the graph data structure in MaMuT can handle efficiently up to about a hundred thousand annotations. This number is well within the realm of manually generated annotations, but is normally exceeded by large-scale fully automated lineaging engines like TGMM. As a trade-off until this constraint is addressed in the future, we also provide users the option to crop the

511 imported TGMM annotations in space and/or in time to make them compatible with
512 MaMuT.
513
514 The crustacean *Parhyale* is already an attractive new model for developmental genetic
515 and functional genomic studies (Kao et al., 2016; Liubicich et al., 2009; Martin et al.,
516 2016; Pavlopoulos et al., 2009; Stamataki and Pavlopoulos, 2016). By extending here the
517 experimental toolkit with multi-view LSFM and cellular reconstructions with MaMuT, it
518 is feasible to study gene expression and function in the context of single-cell resolution
519 fate maps. Especially when it comes to appendage development, the *Parhyale* body plan
520 provides exceptional material to probe the molecular and cellular basis of tissue
521 patterning, growth and differentiation during normal embryogenesis and post-embryonic
522 regeneration (Alwes et al., 2016; Konstantinides and Averof, 2014).
523
524 The tempo and mode of development has also important ramifications for *Parhyale*
525 imaging and tracking. The relatively slow tempo of development enables us to image
526 embryos at a very high spatial resolution through the acquisition of multiple and highly
527 overlapping views without compromising the temporal resolution. *Parhyale* can match
528 the spatiotemporal resolution of *Drosophila* or zebrafish LSFM datasets, even when
529 access to highest-speed instruments is not available. Due to the optical clarity of the
530 embryo and positioning of the appendages on the surface of the developing embryo, all
531 constituent cells can be followed for quantitative analyses. Finally, the stereotyped and
532 ordered organization of the *Parhyale* ectoderm will allow to identify homologous cells
533 and compare lineages, cell behaviors and associated genes between serially homologous
534 structures in the same embryo, across embryos and even across malacostracan
535 crustaceans (Browne et al., 2005; Dohle et al., 2004; Dohle and Scholtz, 1988;
536 Gerberding et al., 2002; Hejnol and Scholtz, 2004; Scholtz, 1990; Scholtz et al., 1994;
537 Wolff and Gerberding, 2015; Wolff and Scholtz, 2002, 2008).
538
539 **Cellular basis of arthropod limb morphogenesis: lessons from *Parhyale***
540 The combination of multi-view light-sheet imaging and tracking has enabled a detailed
541 analysis of the dynamics of all constituent cells in an outgrowing and elongating animal

limb. So far, these descriptions have been only partly available for *Drosophila* limbs that are derived and not representative for many insects, much less arthropods in general, in two very important respects. First, limb specification, patterning, growth and differentiation take place at distinct developmental stages during embryonic, larval and pupal development. On the contrary, all these processes come about during embryogenesis in most other arthropods, including *Parhyale*. In addition to these heterochronic shifts, limb patterning mechanisms in *Drosophila* operate in the flat imaginal disc epithelia, rather than the 3D epithelial outgrowths observed in *Parhyale* that are typical for most other arthropod limbs.

Classical lineaging experiments revealed that tissue compartmentalizations in the *Drosophila* wing and leg primordia take place along the AP axis during early embryogenesis and along the DV axis during larval development (Garcia-Bellido et al., 1973; Steiner, 1976). Our understanding of the AP and DV organization in other arthropod limbs has relied so far entirely on gene expression studies. Expression of segment polarity genes, like *en* and *wingless* (*wg*), has demonstrated that the AP separation is conserved across arthropods and takes place during segmentation (Angelini and Kaufman, 2005; Damen, 2007). In *Parhyale*, the AP compartment boundary is established at the 1-row stage at the interface of neighboring parasegments (Browne et al., 2005; Dohle and Scholtz, 1988; Hejnol and Scholtz, 2004; Scholtz et al., 1994). With the exception of descriptive gene expression studies (Angelini and Kaufman, 2005; Damen, 2007; Janssen et al., 2008), the mechanism, timing and position of the DV separation in arthropod limbs has remained unexplored at the cellular level due to the lack of lineage tracing methodologies. Even in *Drosophila*, it is not entirely clear yet whether DV separation in the leg disc relies on heritable or non-heritable subdivisions or a combination of both mechanisms (Brook and Cohen, 1996; Steiner, 1976; Svendsen et al., 2015).

By analyzing the dynamics of digital clones in reconstructed T2 limbs, we have been able to explore the cellular basis of limb patterning in *Parhyale*. This approach first confirmed the position and timing of the known AP compartment boundary, and then revealed a

putative heritable subdivision along the DV axis from the 4-row-parasegment stage onwards. Interestingly, expression of the *Distal-less* gene, which is an early marker of limb specification, is first detected at the 4-row-parasegment in the d3/d4 cells located at the intersection of the AP and DV boundaries (Browne et al., 2005; Hejnol and Scholtz, 2004). This intersection also marks the tip of the forming limb throughout epithelial remodeling and outgrowth. Thus, the *Parhyale* limb appears to perfectly conform to Meihardt's boundary model (Meinhardt, 1983). This model postulates that a secondary developmental field, i.e. the PD axis of a limb that is specified during embryogenesis *de novo* relative to the main AP and DV body axes, initiates and is patterned around the intersection of the AP and DV compartment boundaries.

The inference of the four constituent compartments provided a powerful framework to interpret the cell behaviors during limb development both in a qualitative and quantitative manner. This analysis strongly suggested that a combination of cellular mechanisms is at work to remodel the embryonic epithelium during limb outgrowth. First, there was a significant difference in cell proliferation rates between the center (faster dividing) and the periphery (slower dividing) of the limb primordium from early specification until limb bud formation. Such a growth-based morphogenesis model has been the dominant hypothesis for almost 50 years to explain the outgrowth of the vertebrate limb (Ede and Law, 1969; Hornbruch and Wolpert, 1970; Morishita and Iwasa, 2008; Searls and Janners, 1971) – oriented cell motion and division were also recently involved (Boehm et al., 2010; Wyngaarden et al., 2010) - but has never been implicated as the driving mechanism behind arthropod limb evagination. Limb bud formation can be reduced by inhibiting cell proliferation pharmacologically, as has been demonstrated in larvae of another crustacean with direct developing limbs, the brine shrimp *Artemia* (Freeman et al., 1992). Second, limb elongation was tightly associated - and presumably effected - by two patterned cell behaviors: i) increased cell proliferation at the tip of the limb resembling a putative growth zone which generates many of the new cells necessary for limb outgrowth, and ii) strong bias in the orientation of mitotic divisions parallel to the PD axis of growth. Third, the different PD domains of the *Parhyale* limb could be traced back to distinct mediolateral positions in the early germband stage. During limb bud

formation and elongation, there was a transition and refinement of these positional values along the PD axis. Fourth, besides the early AP and DV lineage restrictions, we observed a secondary PD separation between neighboring segments during limb segmentation.

Overall, our approach demonstrates that the comprehensive fine-scale reconstruction of a developmental process can shed light into functionally interdependent patterning mechanisms operating across multiple scales.

Reconciling genetic with cellular models of limb morphogenesis

In the *Drosophila* leg disc, the Dpp and Wg ligands are induced at the AP boundary in the dorsal and ventral cells, respectively. Dpp and Wg create a concentration gradient with the highest level in the center of the disc and lower levels towards the periphery, and cooperate in the establishment of concentric domains of gene expression of a set of limb gap genes that pattern the PD axis (Estella et al., 2012). Dpp and Wg signaling also act antagonistically to control dorsal and ventral cell fate through regulation of the downstream selector T-box genes *optomotor blind*/*Doc* dorsally and *H15*/*midline* ventrally (Svendsen et al., 2015).

The PD expression of the limb gap genes is conserved in arthropods, including *Parhyale* (Angelini and Kaufman, 2005; Browne et al., 2005; Prpic and Telford, 2008). Our analysis of *dpp*, *Doc* and *H15* expression in a crustacean species also suggests conserved roles for these genes in dorsal and ventral cell fate specification, and provides extra independent support for a compartment-based mechanism to pattern the DV axis of arthropod limbs. *Wg* expression is currently not known in *Parhyale*. If it is expressed in a complementary pattern to *Ph-dpp* in the prospective ventral territory, it could point to a similar logic for patterning the limb PD axis like in *Drosophila*. In fact, our reconstructions have suggested that the distal DV margin (that in this scenario would experience the highest levels of Dpp and Wg signaling) is located between descendent cells from columns 4 and 5. These are indeed the cells that contribute to the most distal limb segments.

Although the function of the Dpp morphogen gradient in patterning the *Drosophila* limbs is well understood, its role in promoting growth is still controversial (Akiyama and Gibson, 2015; Barrio and Milan, 2017; Bosch et al., 2017; Harmansa et al., 2015; Matsuda and Affolter, 2017; Restrepo et al., 2014; Rogulja and Irvine, 2005). The anterior-dorsal cells expressing *Ph-dpp* and *Ph-Doc* were among the fastest dividing cells in the center of the limb primordium. Later, strong expression of *Ph-dpp* and *Ph-Doc* resolved into a row of cells abutting the AP compartment boundary. Again, these cells displayed some of the highest proliferation rates quantified during limb outgrowth, suggesting a Dpp-dependent control of *Parhyale* limb growth. We anticipate that the LSFM imaging and tracking approaches described here, together with the recent application of CRSIPR/Cas-based methodologies for genome editing (Kao et al., 2016) will provide excellent tools to further explore how morphogens like Dpp regulate growth and form at cellular resolution.

Materials and methods

Key resources table

Reagent type (species) or resource	Designation	Source or reference	Identifiers	Additional information
Strain, strain background (*Parhyale hawaiensis*)	Wild Type	PMID: 15986449		
Strain, strain background (*P. hawaiensis*)	*PhHS>H2B-mRFPruby*	This paper		
Recombinant DNA reagent	pMi{3xP3> EGFP; PhHS>H2B-mRFPruby}	This paper		
Software, algorithm	MaMuT	This paper		http://imagej.net/MaMuT
Software, algorithm	SIMI°BioCell	PMID: 9133433		http://simi.com/en/products/ cell-research
Gene (*P. hawaiensis*)	*Ph-dpp*	This paper	GenBank: KY696711	
Gene (*P.*	*Ph-Doc*	This paper	GenBank:	

hawaiensis)			KY696712	
Gene (*P. hawaiensis*)	*Ph-en2*	This paper	GenBank: KY696713	
Gene (*P. hawaiensis*)	*Ph-H15*	This paper		

651

652 **Generation of transgenic *Parhyale* labeled with H2B-mRFPruby**

653 *Parhyale hawaiensis* (Dana, 1853) rearing, embryo collection, microinjection and
654 generation of transgenic lines were carried out as previously described (Kontarakis and
655 Pavlopoulos, 2014). To fluorescently label the chromatin in transgenic *Parhyale*, we
656 fused the coding sequences of the *Drosophila* histone *H2B* and the *mRFPruby*
657 monomeric Red Fluorescent Protein and placed them under control of a strong *Parhyale*
658 heat-inducible promoter (Pavlopoulos et al., 2009). *H2B* was amplified from genomic
659 DNA with primers Dmel_H2B_F_NcoI (5'-
660 TTAACCATGGCTCCGAAAACTAGTGGAAAG-3') and Dmel_H2B_R_XhoI (5'-
661 ACTTCTCGAGTTTAGAGCTGGTGTACTTGG-3'), and *mRFPruby* was amplified
662 from plasmid pH2B-mRFPruby (Fischer et al., 2006) with primers mRFPruby_F_XhoI
663 (5'-ACAACTCGAGATGGGCAAGCTTACC-3') and mRFPruby_R_PspMOI (5'-
664 TATTGGGCCCTTAGGATCCAGCGCCTGTGC-3'). The NcoI/XhoI-digested H2B and
665 XhoI/PspOMI-digested mRFPruby fragments were cloned in a triple-fragment ligation
666 into NcoI/NotI-digested vector pSL-PhHS>DsRed, placing *H2B-mRFPruby* under
667 control of the *PhHS* promoter (Pavlopoulos et al., 2009). The *PhHS>H2B-mRFPruby-*
668 *SV40polyA* cassette was then excised as an AscI fragment and cloned into the AscI-
669 digested pMinos{3xP3>EGFP} vector (Pavlopoulos and Averof, 2005; Pavlopoulos et
670 al., 2004), generating plasmid pMi{3xP3>EGFP; PhHS>H2B-mRFPruby}. Three
671 independent transgenic lines were established with this construct for heat-inducible
672 expression of H2B-mRFPruby. The most strongly expressing line was selected for all
673 applications. In this line, nuclear H2B-mRFPruby fluorescence plateaued about 12 hours
674 after heat-shock and high levels of fluorescence persisted for at least 24 hours post heat-
675 shock labeling chromatin in all cells throughout the cell cycle.

676

677 **Multi-view LSFM imaging of *Parhyale* embryos**

Standard procedures for multi-view LSFM recordings of *Parhyale* embryogenesis were established after imaging several dozen embryos individually in pilot experiments, first on a Zeiss prototype and, later on, on the commercial Zeiss Lightsheet Z.1 microscope. Several parameters described below were optimized to ensure that the two embryos used for lineage reconstruction i) survived the recording process and hatched into juveniles without any morphological abnormalities, and ii) were imaged with the appropriate spatiotemporal resolution and signal-to-noise ratio for accurate and comprehensive cell tracking in developing appendages.

To prepare embryos for LSFM imaging, 2.5-day old transgenic embryos (early germband stage; S11 according to (Browne et al., 2005) were heat-shocked for 1 hour at 37˚C. About 12 hours later (stage S13), they were mounted individually in a cylinder of 1% low melting agarose (SeaPlaque, Lonza) inside a glass capillary (#701902, Brand GmbH) with their AP axis aligned parallel to the capillary. A 1:4000 dilution of red fluorescent beads (#F-Y050 microspheres, Estapor Merck) were included in the agarose as fiducial markers for multi-view reconstruction. During imaging, the embedded embryo was extruded from the capillary into the chamber filled with artificial seawater supplemented with antibiotics and antimycotics (FASWA; (Kontarakis and Pavlopoulos, 2014). The FASWA in the chamber was replaced every 12 hours after each heat shock (see below). The Zeiss Lightsheet Z.1 microscope was equipped with a 20x/1.0 Plan Apochromat immersion detection objective and two 10x/0.2 air illumination objectives producing two light-sheets 5.1 µm thick at the waist and 10.2 µm thick at the edges of a 488 µm x 488 µm field of view.

We started imaging *Parhyale* embryogenesis from 3 angles/views (the ventral side and the two ventral-lateral sides 45˚ apart from ventral view) during 3 to 4.5 days AEL to avoid photo-damaging the dorsal thin extra-embryonic tissue, and continued imaging from 5 views (adding the two lateral sides 90˚ apart from ventral view) during 4.5 to 8 days AEL. A multi-view acquisition was made every 7.5 min at 26˚C. The H2B-mRFPruby fluorescence levels were replenished regularly every 12 hours by raising the temperature in the chamber from 26˚C to 37˚C and heat-shocking the embryo for 1 hour.

Each view (z-stack) was composed of 250 16-bit frames with voxel size 0.254 µm x 0.254 µm x 1 µm. Each 1920x1920 pixel frame was acquired using two pivoting light-sheets to achieve a more homogeneous illumination and reduced image distortions caused by light scattering and absorption across the field of view. Each optical slice was acquired with a 561 nm laser and exposure time of 50 msec. With these conditions, *Parhyale* embryos, like the one bearing the T2 limb#1 analyzed in detail with MaMuT, were imaged routinely for a minimum of 4 days or even up to hatching. After hatching, the morphology of imaged specimen was compared between the left and the right side, as well as to its non-imaged siblings, to confirm that no obvious developmental or morphological abnormalities were detected.

The embryo bearing the T2 limb#2 was imaged on a Zeiss LSFM prototype (Preibisch et al., 2010) that offered single-sided illumination and single-sided detection with a 40x/0.8 immersion objective. One side of this embryo was imaged from 3 views 40˚ apart (ventral, ventral-left and left) every 7.5 min over a period of 66 hours. Each view was composed of 150 frames (1388x1080 pixels) with voxel size 0.366 µm x 0.366 µm x 2 µm. The embryo was imaged at 29-30˚C and was heat-shocked for 1 hour twice a day by perfusing warm FASWA at 37˚C. Cell tracking was carried out with the SIMI°BioCell software (Hejnol and Scholtz, 2004; Schnabel et al., 1997) on a single view, the ventral-left view, of this dataset. Lineage reconstruction of limb#2 with SIMI°BioCell was complete up to about 22 hours of imaging time (35 hours when scaled to the growth rate of limb#1). After this time-point, an increasing number of cells in limb#2, in particular the descendant cells from the medial columns, became intractable.

4D reconstruction of *Parhyale* embryogenesis from multi-view LSFM image datasets

Parhyale LSFM acquisitions typically resulted in 192 time-points / 240K images / 1.7 TB of raw data per day. Image processing was carried out on a MS Windows 7 Professional 64-bit workstation with 2 Intel Xeon E5-2687W processors, 256 GB RAM (16 X DIMMs 16384 MB 1600 MHz ECC DDR3), 4.8 TB hard disk space (2 X 480 GB and 6 X 960 GB Crucial M500 SATA 6Gb/s SSD), 2 NVIDIA Quadro K4000 graphics cards (3 GB GDDR5). The workstation was connected through a 10 GB network interface to a MS

Windows 2008 Server with 2 Intel Xeon E5-2680 processors, 196 GB RAM (24 X DIMM 8192 MB 1600 MHz ECC DDR3) and 144 TB hard disk space (36 X Seagate Constellation ES.3 4000 GB 7200 RPM 128 MB Cache SAS 6.0Gb/s). All major LSFM image data processing steps were done with software modules available through the Multiview Reconstruction Fiji plugin (http://imagej.net/Multiview-Reconstruction) according to the following steps:

1) Preprocessing: Image data acquired on Zeiss Lightsheet Z.1 were saved as an array of czi files labeled with ascending indices, where each file represented one view (z-stack). czi files were first renamed into the "spim_TL{t}_Angle{a}.czi" filename, where t represented the time-point (e.g. 1 to 192 for a 1-day recording) and a the angle (e.g. 0 for left view, 45 for ventral-left view, 90 for ventral view, 135 for ventral-right view and 180 for right view), and then resaved as tif files.

2) Bead-based spatial multi-view registration: In each time-point, each view was aligned to an arbitrary reference view fixed in 3D space (e.g. views 0, 45, 90, 135 aligned to 180) using the bead-based registration option (Preibisch et al., 2010). In each view, fluorescent beads scattered in the agarose were segmented with the Difference-of-Gaussian algorithm using a sigma value of 3 and an intensity threshold of 0.005. Corresponding beads were identified between views and were used to determine the affine transformation model that matched each view to the reference view within each time-point.

3) Fusion by multi-view deconvolution: Spatially registered views were down-sampled twice for time and memory efficient computations during the image fusion step. Input views were then fused into a single output 3D image with a more isotropic resolution using the Fiji plugin for multi-view deconvolution estimated from the point spread function of the fluorescent beads (Preibisch et al., 2014). The same cropping area containing the entire imaged volume was selected for all time-points. In each time-point, the deconvolved fused image was calculated on GPU in blocks of 256x256x256 pixels with 7 iterations of the Efficient Bayesian method regularized with a Tikhonov parameter of 0.0006.

4) Bead-based temporal registration: To correct for small drifts of the embryo over the extended imaging periods (e.g. due to agarose instabilities), we stabilized the fused volume over time using the segmented beads (sigma = 1.8 and intensity threshold =

0.005) for temporal registration with the affine transformation model using an all-to-all matching within a sliding window of 5 time-points.
5) Computation of spatiotemporally registered fused volumes: Using the temporal registration parameters, we generated a stabilized time-series of the fused deconvolved 3D images.
6) 4D rendering: The *Parhyale* embryo was rendered over time from the spatiotemporally registered fused data using Fiji's 3D Viewer.

Lineage reconstruction with the Massive Multi-view Tracker (MaMuT)

MaMuT was developed as a tool for cell lineaging in multi-view LSFM image volumes by enabling to track objects synergistically from all available views. This functionality has a number of advantages. Raw views do not have to be fused into a single volume, which is computationally by far the most demanding step (Preibisch et al., 2014). The users also preserve the original redundancy of the data, which in many cases like in *Parhyale* allows capturing cells from two or more neighboring views that can be interpreted independently for a more accurate analysis. Finally, MaMuT allows users to analyze sub-optimal datasets that cannot be fused properly or may create fusion artifacts. Of course, combining the raw views with a high-quality fused volume is the best available option, especially when handling complex datasets with high cell densities.

While offering multi-view tracking, MaMuT delivers also other important functionalities. First, it is a turnkey software solution with a convenient interface for interactive exploration, annotation and curation of image data. Any image acquired by any microscopy modality that can be opened in Fiji can be also imported into MaMuT. Second, MaMuT offers a highly responsive and interactive navigation through multi-terabyte datasets. Individual z-stacks representing different views, channels and time-points of a multi-dimensional dataset can be displayed independently or in combinations in multiple synced Viewer windows. Third, objects of interest like cells and nuclei (spots) can be selected synergistically from all available Viewers and followed over time to reconstruct their trajectories (tracks) and lineage information. Fourth, the created spots and tracks can be visualized and edited interactively in the Viewers and the TrackScheme

lineage browser, and animated in the 3D Viewer. For visual interpretation of the data, annotations can be colored based on the primary lineage information or derived numerical parameters. Fifth, lineages can be reconstructed in a manual, semi-automated or fully automated manner followed by manual curation if necessary. Sixth, all spot and track information can be exported from MaMuT to other interfaces for more specialized analyses. Seventh, decentralized annotation by multiple users has been made possible by also developing a web service for remote access to large image volumes stored online. Following on the tradition of the Fiji community for open-source distribution of biological image analysis software, MaMuT is provided freely and openly to the community, it is extensively documented and can be customized by other users.

In practical terms, for lineaging purposes, the *Parhyale* multi-view LSFM raw views were registered spatiotemporally and the image data together with the registration parameters were converted into the custom HDF5/XML file formats utilized by the BigDataViewer and MaMuT Fiji plugins. The MaMuT reconstruction of the *Parhyale* T2 limb described in this article required about 10 weeks of dedicated manual cell tracking by an experienced annotator. The raw image data were displayed in Viewer windows and each z-stack was visualized in any desired color and brightness, scale (zoom), translation (position) and rotation (orientation). All Viewer windows were synced based on the calculated registration parameters and shared a common physical coordinate system; upon selecting an object of interest (spot) in one Viewer, the same spot was identified and displayed in all other windows, and its x, y, z position was mapped onto this common physical space. To guarantee the accuracy of our lineage reconstructions, the center of each tracked nucleus was verified in at least two neighboring views and by slicing the data orthogonally in separate Viewer windows. The nuclei contributing to the T2 limb of interest were identified in the first time-point and tracked manually every 5 time-points except during mitosis, in which case we also tracked one time-point before and one after segregation of the daughter chromosomes during anaphase/telophase. The reconstructed trajectories and lineages were also displayed in two additional synced windows, the TrackScheme and the 3D Viewer. The TrackScheme lineage browser and editor displayed the reconstructed cell lineage tree with tracked nuclei represented as nodes

connected by edges over time and cell divisions depicted as split branches in the tree. The 3D Viewer window displayed interactive animations of the spots depicted as spheres and their tracks over time. The spots and the tracks in the Viewer, TrackScheme and 3D Viewer windows could be color-coded by lineage, position and other numerical features to assist visual analysis and interpretation of the data. In addition, all these windows were synced to simultaneously highlight active spots of interest at the selected time-point, greatly facilitating the cell lineaging process.

Comparison of reconstructed lineage trees

For comparative purposes, each reconstructed lineage tree was defined as a set of division times. For example, let's consider a lineage tree *L* that starts with cell *d.* Cell *d* divides at time t_0 giving rise to the two daughter cells $d_1$and d_2. Then d_1 divides at time t_1 giving rise to daughter cells $d_{11}$and d_{12}. Finally, d_{12} divides at time t_{12} giving the daughter cells d_{121} and d_{122}. In this scenario, we define *L* as $L = \{t_0, t_1, t_{12}\}$.

Let's now consider two lineage trees L^x and L^y, where x and y refer to the founder cells whose lineage trees are under comparison (e.g. x corresponds to E4c5 cell from limb#1 and y to E5b6 cell from limb#2). In order to be comparable, these two lineage trees need to be registered temporally. In our study, we performed a linear rescaling by an empirically determined factor of 1.6 to match the increase in cell number between limb#1 and limb#2 that were imaged at different temperatures and exhibited different growth rates.

We then defined $\Delta(L^x, L^y)$ as the distance between the two registered lineage trees. This distance takes into consideration two metrics, the difference in the timing of divisions and the difference in the number of divisions between the two lineages, and is computed in the following way:

$$\Delta(L^x, L^y) = \frac{\delta_t(L^x, L^y)/n_t + \delta_n(L^x, L^y)/n_n}{2}$$

In this equation, $\delta_t(L^x, L^y)$ is the difference in the timing of divisions and $\delta_n(L^x, L^y)$ is the difference in the number of division between the two lineages. n_t and n_n are used to

normalize the two metrics so that their values are comparable. They are defined as the maximum values observed for $\delta_t(L^x, L^y)$ and $\delta_n(L^x, L^y)$ in a given run of pairwise comparisons, i.e. they are the maximum values obtained in the 34x34 comparisons to calculate the distances between the 34 founder cells within limb#1 or within limb#2 or between limb#1 and limb#2.

δ_n is computed as the absolute value of the difference between the respective numbers of divisions in the two lineage trees:

$$\delta_n(L^x, L^y) = |Card(L^x) - Card(L^y)|$$

To calculate δ_t, we first paired the division times between the two lineage trees. For such a pairing $P = \{(t_i^x, t_j^y) \mid t_i^x \in L^x,\ t_j^y \in L^y\}$ the difference in division times $\delta_t(P)$ is computed as follows:

$$\delta_t(P) = \frac{1}{Card(P)} \sum_{(t_i^x, t_j^y) \in P} |t_i^x - t_j^y|$$

The pairing $P^\star$ that minimizes δ_t is used to compute the temporal distance between the lineage trees. Let $\mathcal{P}$ be the set of all possible pairings, then $P^\star$ is defined as followed:

$$P^\star = \underset{P \in \mathcal{P}}{\operatorname{argmin}}\, \delta_t(P)$$

We then define δ_t as $\delta_t = \delta_t(P^\star)$.

Once we computed all the pairwise distances between lineages of the cells under comparison, hierarchical clustering was performed using Ward's method. For the hierarchical clustering in the average *Parhyale* T2 limb, we combined for each founder cell the information from the two limbs. The average lineage tree L_{12}^x of lineage trees $L_1^x = \{t_{11}^x, t_{12}^x, t_{13}^x\}$ and $L_2^x = \{t_{21}^x, t_{22}^x, t_{23}^x, t_{24}^x\}$, where x corresponds to the founder cell x with lineage trees L_1^x in limb#1 and L_2^x in limb#2, is defined as $L_{12}^x = L_1^x \cup L_2^x = \{t_{11}^x, t_{12}^x, t_{13}^x, t_{21}^x, t_{22}^x, t_{23}^x, t_{24}^x\}$. The computation of the pairwise distance Δ between average lineage trees was then performed as described above.

Analysis of gene expression

887 *Parhyale decapentaplegic* (*Ph-dpp*), *Dorsocross* (*Ph-Doc*), *engrailed-2* (*Ph-en2*) and
888 *H15* (*Ph-H15*) genes were identified by BLAST analysis against the *Parhyale*
889 transcriptome and genome (Kao et al., 2016) using the protein sequence of *Drosophila*
890 orthologs as queries. Sequence accession numbers are KY696711 for *Ph-dpp*, KY696712
891 for *Ph-Doc*, and KY696713 for *Ph-en2*. Phylogenetic tree construction was performed
892 with RAxML using the WAG+G model from MAFFT multiple sequence alignments
893 trimmed with trimAl (Stamatakis, 2014). In situ hybridizations were carried out as
894 previously described (Rehm et al., 2009). Stained samples were imaged on a Zeiss 880
895 confocal microscope using the Plan-Apochromat 10x/0.45 and 20x/0.8 objectives. Images
896 were processed using Fiji and Photoshop CS6 (Adobe Systems Inc). For color overlays,
897 the brightfield image of the *Ph-dpp*, *Ph-Doc* or *Ph-H15* BCIP/NBT staining was inverted,
898 false-colored green and merged with the fluorescent signal of the *Ph-en2* FastRed
899 staining in magenta and the nuclear DAPI signal in blue. In order to map gene expression
900 patterns onto cell lineages, the z-stacks from imaged fixed specimens were imported into
901 MaMuT and the manually reconstructed nuclei and annotated gene expression patterns
902 were compared with the corresponding stages of the live imaged and lineaged embryos.
903 This analysis was performed with single-cell accuracy thanks to the well characterized
904 and invariant patterns of cell division across *Parhyale* embryos, the orderly arrangement
905 of cells in the earlier stages analyzed, and the easily identifiable straight boundary
906 between anterior and posterior cells in the later stages analyzed.
907
908 **Acknowledgements**
909 We are grateful to Michael Akam and Gerhard Scholtz for actively supporting the early
910 phases of this project, Stephan Saalfeld for assistance with image rendering, Fernando
911 Amat for his help with importing TGMM annotations into MaMuT, Damian Kao for
912 assistance with phylogenetics, Michalis Averof and Matthew Benton for comments on
913 the manuscript, and Angeliki-Myrto Farmaki for designing the MaMuT logo. C.W. was
914 supported by the Einstein Foundation Berlin grant A-2012_114. J.Y.T. and S.S were
915 supported by intramural funding from the Pasteur Institute and ANR Program Grandes
916 Investissement de l'avenir France BioImaging Consortium. S.P. was supported by core
917 funding from the Max Delbrück Center. T.P. and P.T. were supported by the core funding

from Max Planck Society and the European Research Council Community's FP7 grant agreement 260746. E.S., L.G., P.J.K. and A.P. were supported by the Howard Hughes Medical Institute. A.P. was also supported by an EC Marie Skłodowska-Curie fellowship.

Competing interests

The authors declare that no competing interests exist.

References

Akiyama, T., and Gibson, M.C. 2015. Decapentaplegic and growth control in the developing Drosophila wing. Nature ***527***:375-378. doi: 10.1038/nature15730, PMID: 26550824.

Alwes, F., Enjolras, C., and Averof, M. 2016. Live imaging reveals the progenitors and cell dynamics of limb regeneration. Elife ***5***. doi: 10.7554/eLife.19766, PMID: 27776632.

Alwes, F., Hinchen, B., and Extavour, C.G. 2011. Patterns of cell lineage, movement, and migration from germ layer specification to gastrulation in the amphipod crustacean Parhyale hawaiensis. Dev Biol ***359***:110-123. doi: 10.1016/j.ydbio.2011.07.029, PMID: 21827744.

Amat, F., Hockendorf, B., Wan, Y., Lemon, W.C., McDole, K., and Keller, P.J. 2015. Efficient processing and analysis of large-scale light-sheet microscopy data. Nat Protoc ***10***:1679-1696. doi: 10.1038/nprot.2015.111, PMID: 26426501.

Amat, F., Lemon, W., Mossing, D.P., McDole, K., Wan, Y., Branson, K., Myers, E.W., and Keller, P.J. 2014. Fast, accurate reconstruction of cell lineages from large-scale fluorescence microscopy data. Nat Methods ***11***:951-958. doi: 10.1038/nmeth.3036, PMID: 25042785.

Angelini, D.R., and Kaufman, T.C. 2005. Insect appendages and comparative ontogenetics. Dev Biol ***286***:57-77. doi: 10.1016/j.ydbio.2005.07.006, PMID: 16112665.

Baena-Lopez, L.A., Baonza, A., and Garcia-Bellido, A. 2005. The orientation of cell divisions determines the shape of Drosophila organs. Curr Biol ***15***:1640-1644. doi: 10.1016/j.cub.2005.07.062, PMID: 16169485.

949 Barrio, L., and Milan, M. 2017. Boundary Dpp promotes growth of medial and lateral
950 regions of the Drosophila wing. Elife ***6***. doi: 10.7554/eLife.22013, PMID: 28675372.
951 Boehm, B., Westerberg, H., Lesnicar-Pucko, G., Raja, S., Rautschka, M., Cotterell, J.,
952 Swoger, J., and Sharpe, J. 2010. The role of spatially controlled cell proliferation in
953 limb bud morphogenesis. PLoS Biol ***8***:e1000420. doi: 10.1371/journal.pbio.1000420,
954 PMID: 20644711.
955 Bosch, P.S., Ziukaite, R., Alexandre, C., Basler, K., and Vincent, J.P. 2017. Dpp controls
956 growth and patterning in Drosophila wing precursors through distinct modes of
957 action. Elife ***6***. doi: 10.7554/eLife.22546, PMID: 28675374.
958 Brook, W.J., and Cohen, S.M. 1996. Antagonistic interactions between wingless and
959 decapentaplegic responsible for dorsal-ventral pattern in the Drosophila Leg. Science
960 ***273***:1373-1377. PMID: 8703069.
961 Browne, W.E., Price, A.L., Gerberding, M., and Patel, N.H. 2005. Stages of embryonic
962 development in the amphipod crustacean, Parhyale hawaiensis. Genesis ***42***:124-149.
963 doi: 10.1002/gene.20145, PMID: 15986449.
964 Buckingham, M.E., and Meilhac, S.M. 2011. Tracing cells for tracking cell lineage and
965 clonal behavior. Dev Cell ***21***:394-409. doi: 10.1016/j.devcel.2011.07.019, PMID:
966 21920310.
967 Chaw, R.C., and Patel, N.H. 2012. Independent migration of cell populations in the early
968 gastrulation of the amphipod crustacean Parhyale hawaiensis. Dev Biol ***371***:94-109.
969 doi: 10.1016/j.ydbio.2012.08.012, PMID: 23046627.
970 Chhetri, R.K., Amat, F., Wan, Y., Hockendorf, B., Lemon, W.C., and Keller, P.J. 2015.
971 Whole-animal functional and developmental imaging with isotropic spatial
972 resolution. Nat Methods ***12***:1171-1178. doi: 10.1038/nmeth.3632, PMID: 26501515.
973 Combs, C.A., and Shroff, H. 2017. Fluorescence Microscopy: A Concise Guide to
974 Current Imaging Methods. Curr Protoc Neurosci ***79***:2 1 1-2 1 25. doi:
975 10.1002/cpns.29, PMID: 28398640.
976 Dahmann, C., Oates, A.C., and Brand, M. 2011. Boundary formation and maintenance in
977 tissue development. Nat Rev Genet ***12***:43-55. doi: 10.1038/nrg2902, PMID:
978 21164524.

979 Damen, W.G. 2007. Evolutionary conservation and divergence of the segmentation
980 process in arthropods. Dev Dyn ***236***:1379-1391. doi: 10.1002/dvdy.21157, PMID:
981 17440988.
982 Day, S.J., and Lawrence, P.A. 2000. Measuring dimensions: the regulation of size and
983 shape. Development ***127***:2977-2987. PMID: 10862736.
984 Dohle, W., Gerberding, M., Hejnol, A., and Scholtz, G. (2004). Cell lineage, segment
985 differentiation, and gene expression in crustaceans. In Evolutionary Developmental
986 Biology of Crustacea. G. Scholtz, ed. (Lisse, The Netherlands: A. A. Balkema
987 Publishers).
988 Dohle, W., and Scholtz, G. 1988. Clonal analysis of the crustacean segment: the
989 discordance between genealogical and segmental borders. Development ***104***
990 ***(Suppl)***:147-160.
991 Du, Z., Santella, A., He, F., Tiongson, M., and Bao, Z. 2014. De novo inference of
992 systems-level mechanistic models of development from live-imaging-based
993 phenotype analysis. Cell ***156***:359-372. doi: 10.1016/j.cell.2013.11.046, PMID:
994 24439388.
995 Dufour, A.C., Jonker, A.H., and Olivo-Marin, J.C. 2017. Deciphering tissue
996 morphodynamics using bioimage informatics. Philos Trans R Soc Lond B Biol Sci
997 ***372***. doi: 10.1098/rstb.2015.0512, PMID: 28348249.
998 Dye, N.A., Popovic, M., Spannl, S., Etournay, R., Kainmuller, D., Ghosh, S., Myers,
999 E.W., Julicher, F., and Eaton, S. 2017. Cell dynamics underlying oriented growth of
1000 the Drosophila wing imaginal disc. Development ***144***:4406-4421. doi:
1001 10.1242/dev.155069, PMID: 29038308.
1002 Ede, D.A., and Law, J.T. 1969. Computer simulation of vertebrate limb morphogenesis.
1003 Nature ***221***:244-248. PMID: 5812579.
1004 Estella, C., Voutev, R., and Mann, R.S. 2012. A dynamic network of morphogens and
1005 transcription factors patterns the fly leg. Curr Top Dev Biol ***98***:173-198. doi:
1006 10.1016/B978-0-12-386499-4.00007-0, PMID: 22305163.
1007 Faure, E., Savy, T., Rizzi, B., Melani, C., Stasova, O., Fabreges, D., Spir, R., Hammons,
1008 M., Cunderlik, R., Recher, G., et al. 2016. A workflow to process 3D+time

microscopy images of developing organisms and reconstruct their cell lineage. Nat Commun *7*:8674. doi: 10.1038/ncomms9674, PMID: 26912388.

Fischer, M., Haase, I., Wiesner, S., and Muller-Taubenberger, A. 2006. Visualizing cytoskeleton dynamics in mammalian cells using a humanized variant of monomeric red fluorescent protein. FEBS Lett ***580***:2495-2502. doi: 10.1016/j.febslet.2006.03.082, PMID: 16638577.

Freeman, J.A., Cheshire, L.B., and MacRae, T.H. 1992. Epithelial morphogenesis in developing Artemia: the role of cell replication, cell shape change, and the cytoskeleton. Dev Biol ***152***:279-292. PMID: 1379558.

Garcia-Bellido, A. 1975. Genetic control of wing disc development in Drosophila. Ciba Found Symp ***0***:161-182. PMID: 1039909.

Garcia-Bellido, A., Ripoll, P., and Morata, G. 1973. Developmental compartmentalisation of the wing disk of Drosophila. Nat New Biol ***245***:251-253. PMID: 4518369.

Gerberding, M., Browne, W.E., and Patel, N.H. 2002. Cell lineage analysis of the amphipod crustacean Parhyale hawaiensis reveals an early restriction of cell fates. Development ***129***:5789-5801. PMID: 12421717.

Gonzalez-Gaitan, M., Capdevila, M.P., and Garcia-Bellido, A. 1994. Cell proliferation patterns in the wing imaginal disc of Drosophila. Mech Dev ***46***:183-200. PMID: 7918103.

Hannibal, R.L., Price, A.L., and Patel, N.H. 2012. The functional relationship between ectodermal and mesodermal segmentation in the crustacean, Parhyale hawaiensis. Dev Biol ***361***:427-438. doi: 10.1016/j.ydbio.2011.09.033, PMID: 22037675.

Harmansa, S., Hamaratoglu, F., Affolter, M., and Caussinus, E. 2015. Dpp spreading is required for medial but not for lateral wing disc growth. Nature ***527***:317-322. doi: 10.1038/nature15712, PMID: 26550827.

Heemskerk, I., Lecuit, T., and LeGoff, L. 2014. Dynamic clonal analysis based on chronic in vivo imaging allows multiscale quantification of growth in the Drosophila wing disc. Development ***141***:2339-2348. doi: 10.1242/dev.109264, PMID: 24866118.

Heisenberg, C.P., and Bellaiche, Y. 2013. Forces in tissue morphogenesis and patterning. Cell ***153***:948-962. doi: 10.1016/j.cell.2013.05.008, PMID: 23706734.

1040 Hejnol, A., and Scholtz, G. 2004. Clonal analysis of Distal-less and engrailed expression
1041 patterns during early morphogenesis of uniramous and biramous crustacean limbs.
1042 Dev Genes Evol ***214***:473-485. doi: 10.1007/s00427-004-0424-2, PMID: 15300435.
1043 Hornbruch, A., and Wolpert, L. 1970. Cell division in the early growth and
1044 morphogenesis of the chick limb. Nature ***226***:764-766. PMID: 5443258.
1045 Huisken, J., and Stainier, D.Y. 2009. Selective plane illumination microscopy techniques
1046 in developmental biology. Development ***136***:1963-1975. doi: 10.1242/dev.022426,
1047 PMID: 19465594.
1048 Huisken, J., Swoger, J., Del Bene, F., Wittbrodt, J., and Stelzer, E.H. 2004. Optical
1049 sectioning deep inside live embryos by selective plane illumination microscopy.
1050 Science ***305***:1007-1009. doi: 10.1126/science.1100035, PMID: 15310904.
1051 Ingaramo, M., York, A.G., Hoogendoorn, E., Postma, M., Shroff, H., and Patterson, G.H.
1052 2014. Richardson-Lucy deconvolution as a general tool for combining images with
1053 complementary strengths. Chemphyschem ***15***:794-800. doi:
1054 10.1002/cphc.201300831, PMID: 24436314.
1055 Janssen, R., Feitosa, N.M., Damen, W.G., and Prpic, N.M. 2008. The T-box genes H15
1056 and optomotor-blind in the spiders Cupiennius salei, Tegenaria atrica and
1057 Achaearanea tepidariorum and the dorsoventral axis of arthropod appendages. Evol
1058 Dev ***10***:143-154. doi: 10.1111/j.1525-142X.2008.00222.x, PMID: 18315808.
1059 Kao, D., Lai, A.G., Stamataki, E., Rosic, S., Konstantinides, N., Jarvis, E., Di
1060 Donfrancesco, A., Pouchkina-Stancheva, N., Semon, M., Grillo, M., et al. 2016. The
1061 genome of the crustacean Parhyale hawaiensis, a model for animal development,
1062 regeneration, immunity and lignocellulose digestion. Elife ***5***. doi:
1063 10.7554/eLife.20062, PMID: 27849518.
1064 Keller, P.J. 2013. Imaging morphogenesis: technological advances and biological
1065 insights. Science ***340***:1234168. doi: 10.1126/science.1234168, PMID: 23744952.
1066 Keller, P.J., Schmidt, A.D., Wittbrodt, J., and Stelzer, E.H. 2008. Reconstruction of
1067 zebrafish early embryonic development by scanned light sheet microscopy. Science
1068 ***322***:1065-1069. doi: 10.1126/science.1162493, PMID: 18845710.
1069 Keller, R. 2012. Developmental biology. Physical biology returns to morphogenesis.
1070 Science ***338***:201-203. doi: 10.1126/science.1230718, PMID: 23066066.

1071 Khairy, K., and Keller, P.J. 2011. Reconstructing embryonic development. Genesis
1072 ***49***:488-513. doi: 10.1002/dvg.20698, PMID: 21140407.
1073 Konstantinides, N., and Averof, M. 2014. A common cellular basis for muscle
1074 regeneration in arthropods and vertebrates. Science ***343***:788-791. doi:
1075 10.1126/science.1243529, PMID: 24385602.
1076 Kontarakis, Z., and Pavlopoulos, A. 2014. Transgenesis in non-model organisms: the
1077 case of Parhyale. Methods Mol Biol ***1196***:145-181. doi: 10.1007/978-1-4939-1242-
1078 1_10, PMID: 25151163.
1079 Kretzschmar, K., and Watt, F.M. 2012. Lineage tracing. Cell ***148***:33-45. doi:
1080 10.1016/j.cell.2012.01.002, PMID: 22265400.
1081 Krzic, U., Gunther, S., Saunders, T.E., Streichan, S.J., and Hufnagel, L. 2012. Multiview
1082 light-sheet microscope for rapid in toto imaging. Nat Methods ***9***:730-733. doi:
1083 10.1038/nmeth.2064, PMID: 22660739.
1084 Lawrence, P.A., and Struhl, G. 1996. Morphogens, compartments, and pattern: lessons
1085 from drosophila? Cell ***85***:951-961. PMID: 8674123.
1086 Lecuit, T., and Mahadevan, L. 2017. Morphogenesis one century after On Growth and
1087 Form. Development ***144***:4197-4198. doi: 10.1242/dev.161125, PMID: 29183932.
1088 LeGoff, L., and Lecuit, T. 2015. Mechanical Forces and Growth in Animal Tissues. Cold
1089 Spring Harb Perspect Biol ***8***:a019232. doi: 10.1101/cshperspect.a019232, PMID:
1090 26261279.
1091 Legoff, L., Rouault, H., and Lecuit, T. 2013. A global pattern of mechanical stress
1092 polarizes cell divisions and cell shape in the growing Drosophila wing disc.
1093 Development ***140***:4051-4059. doi: 10.1242/dev.090878, PMID: 24046320.
1094 Liubicich, D.M., Serano, J.M., Pavlopoulos, A., Kontarakis, Z., Protas, M.E., Kwan, E.,
1095 Chatterjee, S., Tran, K.D., Averof, M., and Patel, N.H. 2009. Knockdown of Parhyale
1096 Ultrabithorax recapitulates evolutionary changes in crustacean appendage
1097 morphology. Proc Natl Acad Sci U S A ***106***:13892-13896. doi:
1098 10.1073/pnas.0903105106, PMID: 19666517.
1099 Mann, R.S., and Carroll, S.B. 2002. Molecular mechanisms of selector gene function and
1100 evolution. Curr Opin Genet Dev ***12***:592-600. PMID: 12200165.

1101 Mao, Y., Tournier, A.L., Hoppe, A., Kester, L., Thompson, B.J., and Tapon, N. 2013.
1102 Differential proliferation rates generate patterns of mechanical tension that orient
1103 tissue growth. EMBO J ***32***:2790-2803. doi: 10.1038/emboj.2013.197, PMID:
1104 24022370.
1105 Martin, A., Serano, J.M., Jarvis, E., Bruce, H.S., Wang, J., Ray, S., Barker, C.A.,
1106 O'Connell, L.C., and Patel, N.H. 2016. CRISPR/Cas9 Mutagenesis Reveals Versatile
1107 Roles of Hox Genes in Crustacean Limb Specification and Evolution. Curr Biol
1108 ***26***:14-26. doi: 10.1016/j.cub.2015.11.021, PMID: 26687626.
1109 Matsuda, S., and Affolter, M. 2017. Dpp from the anterior stripe of cells is crucial for the
1110 growth of the Drosophila wing disc. Elife ***6***. doi: 10.7554/eLife.22319, PMID:
1111 28675373.
1112 Meinhardt, H. 1983. Cell determination boundaries as organizing regions for secondary
1113 embryonic fields. Dev Biol ***96***:375-385. PMID: 6832478.
1114 Milan, M., and Cohen, S.M. 2000. Subdividing cell populations in the developing limbs
1115 of Drosophila: do wing veins and leg segments define units of growth control? Dev
1116 Biol ***217***:1-9. doi: 10.1006/dbio.1999.9493, PMID: 10625531.
1117 Morishita, Y., and Iwasa, Y. 2008. Growth based morphogenesis of vertebrate limb bud.
1118 Bull Math Biol ***70***:1957-1978. doi: 10.1007/s11538-008-9334-1, PMID: 18668295.
1119 Patel, N.H., Kornberg, T.B., and Goodman, C.S. 1989. Expression of engrailed during
1120 segmentation in grasshopper and crayfish. Development ***107***:201-212. PMID:
1121 2632219.
1122 Pavlopoulos, A., and Averof, M. 2005. Establishing genetic transformation for
1123 comparative developmental studies in the crustacean Parhyale hawaiensis. Proc Natl
1124 Acad Sci U S A ***102***:7888-7893. doi: 10.1073/pnas.0501101102, PMID: 15911760.
1125 Pavlopoulos, A., Berghammer, A.J., Averof, M., and Klingler, M. 2004. Efficient
1126 transformation of the beetle Tribolium castaneum using the Minos transposable
1127 element: quantitative and qualitative analysis of genomic integration events. Genetics
1128 ***167***:737-746. doi: 10.1534/genetics.103.023085, PMID: 15238525.
1129 Pavlopoulos, A., Kontarakis, Z., Liubicich, D.M., Serano, J.M., Akam, M., Patel, N.H.,
1130 and Averof, M. 2009. Probing the evolution of appendage specialization by Hox gene

misexpression in an emerging model crustacean. Proc Natl Acad Sci U S A ***106***:13897-13902. doi: 10.1073/pnas.0902804106, PMID: 19666530.

Pietzsch, T., Saalfeld, S., Preibisch, S., and Tomancak, P. 2015. BigDataViewer: visualization and processing for large image data sets. Nat Methods ***12***:481-483. doi: 10.1038/nmeth.3392, PMID: 26020499.

Preibisch, S., Amat, F., Stamataki, E., Sarov, M., Singer, R.H., Myers, E., and Tomancak, P. 2014. Efficient Bayesian-based multiview deconvolution. Nat Methods ***11***:645-648. doi: 10.1038/nmeth.2929, PMID: 24747812.

Preibisch, S., Saalfeld, S., Schindelin, J., and Tomancak, P. 2010. Software for bead-based registration of selective plane illumination microscopy data. Nat Methods ***7***:418-419. doi: 10.1038/nmeth0610-418, PMID: 20508634.

Prpic, N.M., and Telford, M.J. 2008. Expression of homothorax and extradenticle mRNA in the legs of the crustacean Parhyale hawaiensis: evidence for a reversal of gene expression regulation in the pancrustacean lineage. Dev Genes Evol ***218***:333-339. doi: 10.1007/s00427-008-0221-4, PMID: 18504609.

Rehm, E.J., Hannibal, R.L., Chaw, R.C., Vargas-Vila, M.A., and Patel, N.H. 2009. In situ hybridization of labeled RNA probes to fixed Parhyale hawaiensis embryos. Cold Spring Harb Protoc ***2009***:pdb prot5130. doi: 10.1101/pdb.prot5130, PMID: 20147025.

Resino, J., Salama-Cohen, P., and Garcia-Bellido, A. 2002. Determining the role of patterned cell proliferation in the shape and size of the Drosophila wing. Proc Natl Acad Sci U S A ***99***:7502-7507. doi: 10.1073/pnas.072208199, PMID: 12032312.

Restrepo, S., Zartman, J.J., and Basler, K. 2014. Coordination of patterning and growth by the morphogen DPP. Curr Biol ***24***:R245-255. doi: 10.1016/j.cub.2014.01.055, PMID: 24650915.

Rogulja, D., and Irvine, K.D. 2005. Regulation of cell proliferation by a morphogen gradient. Cell ***123***:449-461. doi: 10.1016/j.cell.2005.08.030, PMID: 16269336.

Rubio-Guivernau, J.L., Gurchenkov, V., Luengo-Oroz, M.A., Duloquin, L., Bourgine, P., Santos, A., Peyrieras, N., and Ledesma-Carbayo, M.J. 2012. Wavelet-based image fusion in multi-view three-dimensional microscopy. Bioinformatics ***28***:238-245. doi: 10.1093/bioinformatics/btr609, PMID: 22072386.

1162 Schiegg, M., Hanslovsky, P., Haubold, C., Koethe, U., Hufnagel, L., and Hamprecht,
1163 F.A. 2015. Graphical model for joint segmentation and tracking of multiple dividing
1164 cells. Bioinformatics ***31***:948-956. doi: 10.1093/bioinformatics/btu764, PMID:
1165 25406328.
1166 Schindelin, J., Arganda-Carreras, I., Frise, E., Kaynig, V., Longair, M., Pietzsch, T.,
1167 Preibisch, S., Rueden, C., Saalfeld, S., Schmid, B., et al. 2012. Fiji: an open-source
1168 platform for biological-image analysis. Nat Methods ***9***:676-682. doi:
1169 10.1038/nmeth.2019, PMID: 22743772.
1170 Schmid, B., Shah, G., Scherf, N., Weber, M., Thierbach, K., Campos, C.P., Roeder, I.,
1171 Aanstad, P., and Huisken, J. 2013. High-speed panoramic light-sheet microscopy
1172 reveals global endodermal cell dynamics. Nat Commun ***4***:2207. doi:
1173 10.1038/ncomms3207, PMID: 23884240.
1174 Schmied, C., Stamataki, E., and Tomancak, P. 2014. Open-source solutions for SPIMage
1175 processing. Methods Cell Biol ***123***:505-529. doi: 10.1016/B978-0-12-420138-
1176 5.00027-6, PMID: 24974045.
1177 Schmied, C., Steinbach, P., Pietzsch, T., Preibisch, S., and Tomancak, P. 2016. An
1178 automated workflow for parallel processing of large multiview SPIM recordings.
1179 Bioinformatics ***32***:1112-1114. doi: 10.1093/bioinformatics/btv706, PMID: 26628585.
1180 Schnabel, R., Hutter, H., Moerman, D., and Schnabel, H. 1997. Assessing normal
1181 embryogenesis in Caenorhabditis elegans using a 4D microscope: variability of
1182 development and regional specification. Dev Biol ***184***:234-265. doi:
1183 10.1006/dbio.1997.8509, PMID: 9133433.
1184 Scholtz, G. 1990. The formation, differentiation and segmentation of the post-naupliar
1185 germ band of the amphipod Gammarus pulex L. (Crustacea, Malacostraca,
1186 Peracardida). Proc R Soc Lond B ***239***:163-211.
1187 Scholtz, G., Patel, N.H., and Dohle, W. 1994. Serially homologous engrailed stripes are
1188 generated via different cell lineages in the germ band of amphipod crustaceans
1189 (Malacostraca, Peracarida). Int J Dev Biol ***38***:471-478. PMID: 7848831.
1190 Searls, R.L., and Janners, M.Y. 1971. The initiation of limb bud outgrowth in the
1191 embryonic chick. Dev Biol ***24***:198-213. PMID: 5553367.

1192 Spanjaard, B., and Junker, J.P. 2017. Methods for lineage tracing on the organism-wide
1193 level. Curr Opin Cell Biol ***49***:16-21. doi: 10.1016/j.ceb.2017.11.004, PMID:
1194 29175321.
1195 Stamataki, E., and Pavlopoulos, A. 2016. Non-insect crustacean models in developmental
1196 genetics including an encomium to Parhyale hawaiensis. Curr Opin Genet Dev
1197 ***39***:149-156. doi: 10.1016/j.gde.2016.07.004, PMID: 27475080.
1198 Stamatakis, A. 2014. RAxML version 8: a tool for phylogenetic analysis and post-
1199 analysis of large phylogenies. Bioinformatics ***30***:1312-1313. doi:
1200 10.1093/bioinformatics/btu033, PMID: 24451623.
1201 Stegmaier, J., Amat, F., Lemon, W.C., McDole, K., Wan, Y., Teodoro, G., Mikut, R., and
1202 Keller, P.J. 2016. Real-Time Three-Dimensional Cell Segmentation in Large-Scale
1203 Microscopy Data of Developing Embryos. Dev Cell ***36***:225-240. doi:
1204 10.1016/j.devcel.2015.12.028, PMID: 26812020.
1205 Steiner, E. 1976. Establishment of compartments in the developing leg imaginal discs of
1206 Drosophila melanogaster. Wilhelm Roux Arch. Dev. Biol. ***180***:9-30. doi:
1207 10.1007/BF00848882, PMID: 28304893.
1208 Strassburger, K., Lorbeer, F.K., Lutz, M., Graf, F., Boutros, M., and Teleman, A.A. 2017.
1209 Oxygenation and adenosine deaminase support growth and proliferation of ex vivo
1210 cultured Drosophila wing imaginal discs. Development ***144***:2529-2538. doi:
1211 10.1242/dev.147538, PMID: 28526754.
1212 Sulston, J.E., Schierenberg, E., White, J.G., and Thomson, J.N. 1983. The embryonic cell
1213 lineage of the nematode Caenorhabditis elegans. Dev Biol ***100***:64-119. PMID:
1214 6684600.
1215 Svendsen, P.C., Ryu, J.R., and Brook, W.J. 2015. The expression of the T-box selector
1216 gene midline in the leg imaginal disc is controlled by both transcriptional regulation
1217 and cell lineage. Biol Open ***4***:1707-1714. doi: 10.1242/bio.013565, PMID: 26581591.
1218 Swoger, J., Verveer, P., Greger, K., Huisken, J., and Stelzer, E.H. 2007. Multi-view
1219 image fusion improves resolution in three-dimensional microscopy. Opt Express
1220 ***15***:8029-8042. PMID: 19547131.
1221 Tinevez, J.Y., Perry, N., Schindelin, J., Hoopes, G.M., Reynolds, G.D., Laplantine, E.,
1222 Bednarek, S.Y., Shorte, S.L., and Eliceiri, K.W. 2016. TrackMate: an open and

1223 extensible platform for single-particle tracking. Methods. doi:
1224 10.1016/j.ymeth.2016.09.016, PMID: 27713081.
1225 Tinevez, J.Y., Pietzsch, T., and Rueden, C. 2018. MaMuT. Github.
1226 https://github.com/fiji/MaMuT. 2af9e18.
1227 Tomer, R., Khairy, K., Amat, F., and Keller, P.J. 2012. Quantitative high-speed imaging
1228 of entire developing embryos with simultaneous multiview light-sheet microscopy.
1229 Nat Methods ***9***:755-763. doi: 10.1038/nmeth.2062, PMID: 22660741.
1230 Truong, T.V., Supatto, W., Koos, D.S., Choi, J.M., and Fraser, S.E. 2011. Deep and fast
1231 live imaging with two-photon scanned light-sheet microscopy. Nat Methods ***8***:757-
1232 760. doi: 10.1038/nmeth.1652, PMID: 21765409.
1233 Tsao, C.K., Ku, H.Y., Lee, Y.M., Huang, Y.F., and Sun, Y.H. 2016. Long Term Ex Vivo
1234 Culture and Live Imaging of Drosophila Larval Imaginal Discs. PLoS One
1235 ***11***:e0163744. doi: 10.1371/journal.pone.0163744, PMID: 27685172.
1236 Ulman, V., Maska, M., Magnusson, K.E.G., Ronneberger, O., Haubold, C., Harder, N.,
1237 Matula, P., Matula, P., Svoboda, D., Radojevic, M., et al. 2017. An objective
1238 comparison of cell-tracking algorithms. Nat Methods ***14***:1141-1152. doi:
1239 10.1038/nmeth.4473, PMID: 29083403.
1240 Weber, M., Mickoleit, M., and Huisken, J. 2014. Light sheet microscopy. Methods Cell
1241 Biol ***123***:193-215. doi: 10.1016/B978-0-12-420138-5.00011-2, PMID: 24974029.
1242 Weigmann, K., and Cohen, S.M. 1999. Lineage-tracing cells born in different domains
1243 along the PD axis of the developing Drosophila leg. Development ***126***:3823-3830.
1244 PMID: 10433911.
1245 Wolff, C., and Gerberding, M. (2015). "Crustacea": Comparative Aspects of Early
1246 Development. In Ecdysozoa II: Crustacea. A. Wanninger, ed. (Wien, Austria:
1247 Springer-Verlag).
1248 Wolff, C., and Scholtz, G. 2002. Cell lineage, axis formation, and the origin of germ
1249 layers in the amphipod crustacean Orchestia cavimana. Dev Biol ***250***:44-58. PMID:
1250 12297095.
1251 Wolff, C., and Scholtz, G. 2008. The clonal composition of biramous and uniramous
1252 arthropod limbs. Proc Biol Sci ***275***:1023-1028. doi: 10.1098/rspb.2007.1327, PMID:
1253 18252674.

Worley, M.I., Setiawan, L., and Hariharan, I.K. 2013. TIE-DYE: a combinatorial marking system to visualize and genetically manipulate clones during development in Drosophila melanogaster. Development ***140***:3275-3284. doi: 10.1242/dev.096057, PMID: 23785055.

Wu, Y., Chandris, P., Winter, P.W., Kim, E.Y., Jaumouille, V., Kumar, A., Guo, M., Leung, J.M., Smith, C., Rey-Suarez, I., et al. 2016. Simultaneous multiview capture and fusion improves spatial resolution in wide-field and light-sheet microscopy. Optica ***3***:897-910. doi: 10.1364/OPTICA.3.000897, PMID: 27761486.

Wu, Y., Wawrzusin, P., Senseney, J., Fischer, R.S., Christensen, R., Santella, A., York, A.G., Winter, P.W., Waterman, C.M., Bao, Z., et al. 2013. Spatially isotropic four-dimensional imaging with dual-view plane illumination microscopy. Nat Biotechnol ***31***:1032-1038. doi: 10.1038/nbt.2713, PMID: 24108093.

Wyngaarden, L.A., Vogeli, K.M., Ciruna, B.G., Wells, M., Hadjantonakis, A.K., and Hopyan, S. 2010. Oriented cell motility and division underlie early limb bud morphogenesis. Development ***137***:2551-2558. doi: 10.1242/dev.046987, PMID: 20554720.

Zartman, J., Restrepo, S., and Basler, K. 2013. A high-throughput template for optimizing Drosophila organ culture with response-surface methods. Development ***140***:667-674. doi: 10.1242/dev.088872, PMID: 23293298.

Figure legends

Figure 1. Reconstruction of *Parhyale* embryogenesis with multi-view LSFM (see also Figure 1—videos 1 and 2)

(A) Transgenic *Parhyale* embryo with H2B-mRFPruby-labeled nuclei mounted with fluorescent beads (green dots) for multi-view reconstruction. The embryo was imaged from the indicated 5 views with 45˚ rotation around the AP axis between neighboring views. Panels show renderings of the acquired views with anterior to the left. (B) Raw views were registered and fused into an output image rendered here in different positions around the DV axis. (C-K) Each panel shows a rendering of the embryo at the indicated developmental stage in hours (h) after egg-lay (AEL) and the corresponding time-point (TP) of the recording. Anterior is to the left and dorsal to the top. Abbreviations: first

antenna (An1), second antenna (An2), mandible (Mn), maxilla 1 (Mx1), maxilla 2 (Mx2), thoracic appendages 1 to 8 (T1-T8), pleonic (abdominal) appendages 1 to 6 (P1-P6) and telson (Te). Color masks indicate the cells contributing to Mx2 (blue), T1 (green), T2 and T3 (light and dark yellow) and T4 limb (magenta). (C) Embryo at mid-germband stage S13 according to (Browne et al., 2005). The ventral midline is denoted with the dotted line. (D) S15 embryo. Germband has extended to the posterior egg pole and the first antennal bud is visible anteriorly. (E) S18 embryo with posterior flexure. Head and thoracic appendages have bulged out up to T4. (F) S19 embryo with prominent head and thoracic appendage buds up to T6. (G) S20 embryo continues axial elongation ventrally and anteriorly. Appendage buds are visible up to P3. (H) S21 embryo. Segmentation is complete and all appendages have formed. The Mx2 has split into two branches (blue arrowheads) and the T1 limb has developed two proximal ventral outgrowths (green arrowheads). (I) Embryo at stage S22, (J) S23, and (K) S24 showing different phases of appendage segmentation. Dorsal outgrowths at the base of thoracic appendages, namely coxal plates (orange arrowheads) and gills (red arrowheads), are indicated in T2, T3 and T4. Scale bars are 100 μm.

Figure 2. Grid architecture of the *Parhyale* germband

(A–A'') Rendering of a *Parhyale* embryo at the growing germband stage: (A) Right, (A') ventral, and (A'') left side. Color masks indicate the anterior head region (blue), the bilaterally symmetric midgut precursors (green), the orderly arranged parasegments E1 to E9 (in alternating cyan and magenta), the posterior end of the germband with ongoing organization of cells into new rows (blue), and the extra-embryonic tissue (white). (B-D) Ventral views of elongating germband at the indicated hours (h) after egg-lay (AEL). Ectodermal cells of the E8 parasegment are shown in magenta. (B') Schematics of tracked E8 abcd cells (blue) in the 1-row-parasegment, (C') anterior ab cells (orange) and posterior cd cells (red) after the first longitudinally-oriented division in the 2-row-parasegment, and (D') a (cyan), b (yellow), c (green) and d cells (magenta) after the second longitudinally-oriented division in the 4-row-parasegment. Both mitotic waves proceed in medial-to-lateral direction. The resulting daughter cells sort in clearly defined

columns that are identified by ascending index numbers with 0 denoting the ventral midline and 1, 2, 3 etc. the more lateral columns with increasing distance from midline.

Figure 3. Cell tracking and lineage reconstruction with MaMuT (see also Figure 3—figure supplement 1)

(A) Workflow for image data analysis with MaMuT. Raw views (colored boxes in Multi-view Dataset) are registered (overlapping boxes in Multi-view Registration) and, optionally, fused into a single volume (large cube in Multi-view Fusion). The raw (and fused) image data together with the registration parameters are imported into MaMuT (mammoth logo). In its simplest implementation, all data analysis is done with MaMuT in Fiji workspace. In more advanced implementations, automated segmentation and tracking annotations (yellow point cloud of tracked cells) can be computed separately and imported into MaMuT. The reconstructed lineage information can be exported from MaMuT in an xml file for specialized analyses in other platforms. (B–D) The MaMuT Viewer windows display the raw image data and annotations. All tracked nuclei are marked with magenta circles (in view) or dots (out of view). The active selection is marked in green in all synced Viewers: (B) xy, (B') xz, and (B'') yz plane of first view in cyan; (C) xy plane of second view in yellow; (D) xy plane of third view in blue. (E) The TrackScheme lineage browser and editor where tracks are arranged horizontally and time-points vertically. Tracked objects can be displayed simply as spots (left track) or with extra information like their names and thumbnails (right track). Tracks are displayed as vertical links. The TrackScheme is synced with the Viewer windows; the selected nucleus in panels B–D is also highlighted here in green at the indicated time-point (called frame). Objects can be tracked between consecutive time-points or in larger steps. (F–H) The 3D Viewer window displays interactive animations of tracked objects depicted as spheres. Spots and tracks can be color-coded by lineage, position and other numerical parameters extracted from the data. (F) Digital clone of a nucleus (shown in green) tracked from the grid stage to the limb bud stage. All other tracked nuclei are shown in magenta. (G) Spots color-coded by displacement and tracks color-coded by velocity. (H) Tracked nuclei in the limb bud mapped out in different colors based on z-position. In

panels B–E and H, the selected nucleus and the neighboring dividing nucleus are indicated with green and magenta arrowheads, respectively.

Figure 4. Early compartmentalization of the *Parhyale* thoracic limb (see also Figure 4—figure supplements 1 and 2)

(A–E) Lateral views of a *Parhyale* embryo rendered at the indicated developmental stages shown in hours (h) after egg-lay (AEL). Yellow masks show the left T2 limb (limb#1). (F-J') Tracked cells contributing to limb#1 were color-coded by their compartmental identity: Anterior-Dorsal (dark green), Anterior-Ventral (dark magenta), Posterior-Dorsal (light green), and Posterior-Ventral (light magenta). (F) Ventral view of limb primordium at 84 h AEL made up by cells from the E4 and E5 parasegments. Horizontal lines separate AP rows a to d and vertical lines separate DV columns 3 to 9. (F') Posterior view, rotated 90˚ relative to F. (G) Ventral view of the limb during early eversion at 96 h AEL. (G') Posterior view, rotated 90˚ relative to G. The cells close to the intersection of the four compartments (yellow arrows) are the first to rise above the level of the epithelium. (H–J) Dorsal views of (H) limb bud at 103 h AEL, (I) initial limb elongation at 114 h AEL and (J) later elongation phase at 123 h AEL. (H') Posterior view, rotated 90˚ relative to H, and (I'–J') ventral views, rotated 180˚ relative to I-J. The intersection of the AP and DV boundaries (yellow arrows) is located at the tip of the limb.

Figure 5. Stereotyped and variable cell behaviors in developing *Parhyale* thoracic limbs (see also Figure 5—figure supplement 1, Figure 5—source data 1, and Figure 5—video 1)

(A–C) Schematic representations of the T2 limb primordium at the 4-row-parasegment stage displaying the 34 founder cells as squares color-coded based on their relative birth times: (A) limb#1, (B) limb#2 and (C) their average. The first forming E4c3/d3 cells are colored in black (0% birth time difference), the last forming E5a9/b9 cells in light gray (100% birth time difference) and all other cells in intermediate grayscale shades based on their birth time difference relative to E4c3/d3. (D) Change in cell number over time in limb#1 (blue line) imaged at 26˚C and in the faster developing limb#2 (orange lines)

imaged at 29-30˚C. The first division of the E4cd3 cell is the starting point for both growth curves. Solid lines show the raw data for the two limbs, while the dashed orange line shows the temporally registered data for limb#2. Arrowheads indicate the unscaled and scaled time-point up to which the SIMI°BioCell reconstruction of limb#2 was complete. An increasing number of cells in limb#2 were not possible to track after this time-point resulting in a poor registration with the growth curve of limb#1.

Figure 6. Differential cell proliferation rates in the *Parhyale* thoracic limb (see also Figure 6—figure supplements 1 and 2)

(A–D) Lateral views of the same *Parhyale* embryo shown in Figure 4. (E-H') Tracked cells in limb#1 were color-coded by their average cell cycle length according to the scale (in hours) shown at the bottom. AP and DV boundaries are indicated by the cyan and green line, respectively. Cells for which measurements are not applicable are shown in gray. (E) Ventral view of the limb primordium at 84 hours (h) after egg-lay (AEL). Some central c and d cells start dividing faster at the 4-row-parasegment. (F) Ventral view of the limb during early eversion at 96 h AEL with the middle cells dividing faster than peripheral cells. (G) Dorsal view of limb bud at 103 h AEL. Higher proliferation rates are detected at the tip and in the anterior-dorsal compartment. (H) Dorsal and (H') ventral view of elongating limb at 114 h AEL. Cells at the tip of the limb and anterior cells abutting the AP compartment boundary divide the fastest.

Figure 7. Lineage comparisons within and across *Parhyale* thoracic limbs (see also Figure 7—source data 1)

(A) Hierarchical clustering of the 34 founder cells in the *Parhyale* T2 limb based on a distance matrix computed from their average division patterns in limb#1 and limb#2. The cluster of E4c3-c7 and E4d3-d7 cells at the bottom is shown in blue, the middle cluster containing primarily the E4 and E5 b cells is shown in red, and the top cluster with the remaining cells is shown in magenta. (B,C) Hierarchical clustering of the 34 founder cells in (B) limb#1 and (C) limb#2 based on distance matrices computed from the division patterns observed in each limb. The cells in the two trees (color-coded as in A) display very similar clustering profiles. Heat maps show the timing and number of divisions in 5

time-point-windows. For each founder cell, divisions are represented with rectangles color-coded according to the number of divisions shown in the color bar. The x-axis shows the unscaled tracking time for each limb starting from division of the E4cd3 cell and the white line indicates the time-point at which cells were compared. (D) Box plots showing the distribution of lineage distances in pairwise comparisons between non-homologous (left) and homologous (right) founder cells across the two limbs. The two distributions differ significantly at $p \leq 0.01$ based on the Kolmogorov-Smirnov test. The data used for limbs #1 and #2 in panels A and D were at a comparable stage of their development indicated with the arrowheads in Figure 5D.

Figure 8. Oriented cell divisions in the *Parhyale* thoracic limb

(A–E) Cells in the T2 limb#1 shown at the indicated hours (h) after egg-lay (AEL) color-coded by the orientation of mitotic divisions relative to the AP boundary (cyan line). The AP boundary is parallel to and an accurate proxy for the PD axis during limb outgrowth. The absolute values of the division angle relative to the AP boundary are sorted in 6 bins of 15˚. Gray cells in panel A indicate non-divided cells. (F–J) Rose diagrams with 15˚ intervals showing the percentage of mitotic events falling in each bin color-coded as in A-E (n shows the actual number of divisions). (A,F) Only longitudinally-oriented divisions (perpendicular to the AP boundary) are detected in the limb primordium 73 to 84 h AEL. (B,G) Most cells still divide longitudinally 84 to 96 h AEL, but an increasing number of dividing cells align parallel to the AP boundary during early eversion. (C,H) More than 59% of cells divide 0˚-30˚ relative to the AP boundary in the limb bud from 96 to 103 h AEL. (D,I) Early and (E,J) later limb elongation phase from 103 to 123 h AEL with the large majority of cells (>68%) dividing 0˚-30˚ relative to the AP boundary.

Figure 9. Elaboration of the *Parhyale* limb PD axis (see also Figure 9—figure supplement 1)

(A–F) Rendering of the T2 limb#1 at the indicated hours (h) after egg-lay (AEL). The cells contributing to the T2 primordium are shown in cyan in panel A. Magenta dots indicate the tracked cells E5a5-a8 and their descendants. Panel A shows a ventral view of the germband and panels B–F posterior views of the T2 limb. (G–L) Same stages as in

A–F with color masks showing (G) the limb primordium, (H) the early limb bud, (I) the 2-partite limb with the first subdivision between ischium/merus, (J) the 3-partite limb after the second subdivision between basis/ischium, (K) the 6-partite limb after 3 more subdivisions between coxa/basis, propodus/dactylus and carpus/propodus, and (L) the final pattern made of 7 segments after the carpus/merus division. Colored lines indicate the relationships between limb parts in consecutive stages. (M–R) Schematics of limb subdivisions along the PD axis at the same time-points as in panels G–L. The rectangular lattice in panel M shows the 9 columns of cells in the 4-row-parasegment. White lines in panels N–R delineate the subdivisions of the T2 limb. The origin of each of the 7 limb segments is shown with discs color-coded by segment.

Figure 10. Analysis of developmental regulatory genes corroborates cellular models of limb morphogenesis (see also Figure 10—figure supplement 1)

(A–F) Brightfield images of T2, T3 and T4 limbs from S16-S18 embryos (top row, 84-96 hours AEL) and S19 embryos (bottom row, 96-108 hours AEL) stained by in situ hybridization for *Ph-dpp* (left columns), *Ph-Doc* (middle columns) and *Ph-H15* (right columns). (A'–F') Same limbs as in panels A–F with the nuclear DAPI staining in blue overlaid with the *Ph-dpp*, *Ph-Doc* or *Ph-H15* pattern false-colored in green. Embryos stained for *Ph-Doc* were co-hybridized with *Ph-en2* shown in magenta to label the posterior compartment. (A''–F'') MaMuT reconstructions of the T2 limbs shown in panels A–F. The top panels are color-coded by gene expression with *Ph-dpp*, *Ph-Doc* or *Ph-H15* expressing cells shown in green and non-expressing cells in blue. Bottom panels indicate the identity of the same cells; cells are color-coded by AP rows, column number is shown at the top and white lines connect sister cells. All panels show ventral views with anterior to the top and ventral midline to the left. Scale bars are 20 μm.

Supplemental figure legends

Figure 3—figure supplement 1. MaMuT layout

(A–C) The three tabs of the MaMuT control panel. (A) The Views tab is used to launch and control the different displays of the image data and annotations. (B) The Annotation tab is used to define the temporal sampling during manual lineaging and the parameters for semi-automated tracking. (C) The Actions tab allows users to generate movies of tracked objects or merge independent MaMuT annotations of the same image dataset into a single file. (D) The Visibility and Grouping panel allows users to organize views into groups and display them overlaid in the same Viewer window. (E) The Brightness and Color panel is used to adjust brightness, contrast and color of the image data in the Viewer windows. For example, three different views are shown in panels G-L in cyan, blue and yellow, respectively. (F) The MaMuT help menu with the default mouse and keyboard operations that can be modified by the user. (G–L) The MaMuT Viewer windows display the raw image data. The user interacts with the data to create and edit annotations through these Viewers and the TrackScheme window. The user can open as many Viewer windows as required for accurate tracking, and can display the image data in any useful scale, position and orientation (two orientations shown here per view). (M) The TrackScheme window is the dedicated lineage browser and editor where tracks are arranged from left to right and time-points from top to bottom. (N) The 3D Viewer window shows animations of the tracked objects as spheres without the image data. The TrackScheme, the 3D Viewer and all open Viewer windows are synced (with the active selection highlighted in bright green) and annotations can be color-coded according to various parameters extracted from the data.

Figure 4—figure supplement 1. Lineage reconstruction of the *Parhyale* thoracic limb

(A–E) Lateral views of the same *Parhyale* embryo shown in Figure 4. Yellow masks indicate the left T2 limb (limb#1). (F–J) Tracked cells contributing to the T2 limb color-coded by the DV column they belong to: column 3 in yellow, 4 in orange, 5 in red, 6 in green, 7 in cyan, 8 in blue, and 9 in magenta. Note the cell mixing and irregular clone borders between descendent cells from neighboring columns. (K–O') Tracked cells

contributing to the T2 limb belong to the E4 and E5 parasegments, and are color-coded by the AP row they belong to: a row in cyan, b rows in yellow, c row in green and d row in magenta. Note the absence of cell mixing at the AP compartment boundary between anterior E4d cells (magenta) and posterior E5a cells (cyan), as well as the absence of cell mixing at the presumptive DV boundary between ventral E4b cells (yellow) and dorsal E4c cells (green) anteriorly, and between ventral E5b cells (yellow) and dorsal E5a cells (cyan) posteriorly. (F,K) Ventral views of the limb primordium at 84 hours (h) after egg-lay (AEL). (G,L) Ventral views of the limb during early eversion at 96 h AEL. (H,M) Dorsal views of the limb bud at 103 h AEL. (I,N) Dorsal views of initial limb elongation at 114 h AEL. (J,O) Dorsal views of later elongation phase at 123 h AEL. (M'–O') Ventral views, rotated 180˚ relative to M–O.

Figure 4—figure supplement 2. Independent evidence for early compartmentalization of the *Parhyale* thoracic limb

(A–D) Lateral views of another *Parhyale* embryo imaged on a Zeiss LSFM prototype instrument rendered at the indicated developmental stages shown in hours (h) after egg-lay (AEL). Yellow masks indicate the left T2 limb (limb#2). (E–H') Cells contributing to limb#2 were tracked with the SIMI°BioCell software and were color-coded by their compartmental identity: Anterior-Dorsal (dark green), Anterior-Ventral (dark magenta), Posterior-Dorsal (light green), and Posterior-Ventral (light magenta). (E) Ventral view of the limb primordium at 86 h AEL. Horizontal lines separate AP rows a to d, and vertical lines separate DV columns 3 to 9. (E') Posterior view, rotated 90˚ relative to E. (F) Ventral view of the limb primordium during eversion at 94 h AEL. (F') Posterior view, rotated 90˚ relative to F. The cells close to the intersection of the four compartments (yellow arrows) have risen above the level of the epithelium. (G–H) Dorsal views of limb bud at 98 h AEL and initial limb elongation at 101 h AEL. (G'–H') Ventral views, rotated 180˚ relative to G–H. The intersection of the AP and DV compartment boundaries (yellow arrows) marks the tip of the limb. Limb#2 exhibited the same lineage restrictions like the more completely reconstructed limb#1. Cells in the anterior compartment (E4b, c and d rows) remained together and separate by a straight boundary from the cells in the posterior compartment (E5a and b rows). Likewise, no cell mixing was detected across

the dorsal-ventral compartment boundary that extended again between the E4b and c rows anteriorly, between the E5a and b rows posteriorly, and between cells E4c4-c5, E4d3-d4 and E5a4-a5 medially.

Figure 5—figure supplement 1. Reconstructed lineage tree of a *Parhyale* T2 limb

Each track resembles one or two of the 34 founder cells of limb#1 color-coded by their compartmental identity: anterior-dorsal in dark green, anterior-ventral in dark magenta, posterior-dorsal in light green, and posterior-ventral in light magenta. Tracks labeled with the names of the 34 cells are arranged horizontally and the 400 time-points of tracking time, corresponding to 50 hours of development, are arranged vertically.

Figure 6—figure supplement 1. Digital clonal analysis in the *Parhyale* thoracic limb

Digital clones for each one of the 34 founder cells of the T2 limb#1 visualized at 114 hours (h) after egg-lay (AEL). In each panel, the name of the founder cell is shown in the top left corner and its position in the limb primordium at 84 h AEL is shown in the bottom left corner. The cells of the clone are shown in bright green. The rest cells have been color-coded by their compartmental identity: Anterior-Dorsal in dark green, Anterior-Ventral in dark magenta, Posterior-Dorsal in light green, and Posterior-Ventral in light magenta.

Figure 6—figure supplement 2. Alternative quantifications of cell proliferation rates in the *Parhyale* thoracic limb

(A –E) Tracked cells making up the T2 limb#1 shown at the indicated hours (h) after egg-lay (AEL) and color-coded by their compartmental identity: Anterior-Dorsal in dark green, Anterior-Ventral in dark magenta, Posterior-Dorsal in light green, and Posterior-Ventral in light magenta. (F–J) Same stages as in A–E with cells color-coded by the average cell cycle length of each cell according to the scale shown on the right. (F'–J') Same stages as in A–E with cells color-coded by the absolute cell cycle length of each cell according to the scale shown on the right. (F''–J'') Same stages as in A–E with cells color-coded by the average cell cycle length of each track according to the scale shown on the right. The AP and DV compartment boundaries are indicated by the cyan and

green line, respectively. During the early stages, all analyses - irrespective of the method of quantification - demonstrate that a group of central cells in the limb primordium divide faster compared to peripheral cells. During later stages, the higher cell proliferation rates at the tip of the limb and at the AP compartment boundary are more pronounced with the calculation of the average cell cycle length for each cell. Gray cells indicate cells for which measurements are not applicable.

Figure 9—figure supplement 1. Proximal-distal lineage separation in the growing *Parhyale* thoracic limb

(A–E) Tracked cells contributing to the T2 limb#1 color-coded by their compartmental identity: Anterior-Dorsal (dark green), Anterior-Ventral (dark magenta), Posterior-Dorsal (light green), and Posterior-Ventral (light magenta). (A) Ventral view of the limb primordium at 84 hours (h) after egg-lay AEL. (B) Ventral view of the limb during early eversion at 96 h AEL. (C) Dorsal view of limb bud at 103 h AEL. Posterior views of (D) initial limb elongation at 114 h AEL and (J) later elongation phase at 123 h AEL. (F–J) Same stages and views as in A-E with cells contributing to the proximal (p) leg segments (coxa, basis, and ischium) shown in cyan and cells contributing to the distal (d) leg segments (merus, carpus, propodus, and dactylus) shown in yellow. Progenitor cells giving rise to both proximal and distal leg segments are shown in bright green. (K–M) Later stages of limb segmentation at (K) 132 h AEL, (L) 140 h AEL and (M) 150 h AEL. In these panels, the T2 limb has been rendered in posterior view and superimposed with the tracked cells (descendant cells from posterior-dorsal progenitors E5a5-a8 shown as dots) covering the limb proximal-distal axis. Note that the proximal cells (in cyan) and the distal cells (in yellow) stop mixing at the ischium/merus joint (demarcated with the white line in K–M) after about 110 h AEL. (N) Cell lineage tree of limb#1 where the tracks have been color-coded by their proximal or distal identity: proximal identity in cyan, distal identity in yellow, and mixed identity in green. Proximal and distal cells originate from the peripheral and medial territories of the limb primordium, respectively.

Figure 10—figure supplement 1. Expression of *Ph-dpp*, *Ph-Doc* and *Ph-H15* during *Parhyale* limb bud formation

(A–F) Brightfield images of S16-S18 embryos (top row, 84-96 hours AEL) and S19 embryos (middle row, 96-108 hours AEL) stained by in situ hybridization for *Ph-dpp* (left columns), *Ph-Doc* (middle columns) and *Ph-H15* (right columns). (A'–F') Same embryos as in panels A–F with the nuclear DAPI staining in blue overlaid with the *Ph-dpp*, *Ph-Doc* or *Ph-H15* pattern false-colored in green. Embryos stained for *Ph-Doc* were co-hybridized with *Ph-en2* shown in magenta to label the posterior compartment. Panels show ventral views with anterior to the top. Rectangles indicate the T2, T3 and T4 limbs shown in Figure 10. Scale bars are 100 μm. (G) Phylogenetic analysis of BMP family proteins and (H) T-box transcription factors. Scale bars show number of substitutions per site.

Rich media file legends

Figure 1—video 1. Imaging *Parhyale* embryogenesis with multi-view LSFM

Time-lapse recording of a transgenic embryo from the crustacean amphipod *Parhyale hawaiensis* labeled with the nuclear H2B-mRFPruby fluorescent marker. The embryo was recorded on a Zeiss Lightsheet Z.1 microscope that offers two-sided illumination and single-sided detection with a 20x/1.0 objective. This embryo was imaged from 5 views 45˚ apart (ventral side, the two ventral-lateral sides and two lateral sides) for slightly longer than 4.5 days with a temporal resolution of 7.5 min. Development of the entire embryo was reconstructed from the 5 input views by registering them in space and time using fluorescent beads scattered in the agarose where the embryo was embedded, by fusing the registered views into a single output image with a more isotropic resolution using a multi-view deconvolution algorithm, and by rendering of the fused volume and rotating it around the anterior-posterior x-axis over time. All image-processing steps were carried out with open-source software available in the Fiji image analysis platform. The movie plays 3 hours of *Parhyale* development per second, displaying development 10800 times faster than normal. The movie starts at 3 days AEL, when a distinct germband has formed ventrally and is surrounded by large spaced-out nuclei of extra-embryonic identity. Segment formation and maturation progresses from anterior to posterior and is accompanied by embryo elongation, first posteriorly and later on ventrally and anteriorly. During these stages, the embryo develops a series of specialized appendages along the anterior-posterior axis that can be observed projecting ventrally, elongating and segmenting along their proximal-distal axis. Anterior is to the left.

Figure 1—video 2. Imaging *Parhyale* embryogenesis with multi-view LSFM

Left side of the same embryo shown in Movie S1 rendered with the same settings but without rotation. Anterior is to the left and dorsal to the top.

Figure 5—video 1. Animation of tracked cells forming the *Parhyale* second thoracic limb

All tracked cells contributing to the T2 limb#1 are displayed as spheres of uniform color. The movie starts from the early limb specification stage at about 3 days AEL and covers

limb bud formation and initial elongation over the following 50 hours. This animation was produced with the 3D Viewer of the Massive Multi-view Tracker (MaMuT) plugin in Fiji. The movie plays 5 hours of limb development per second, displaying *Parhyale* limb development 18000 times faster than normal.

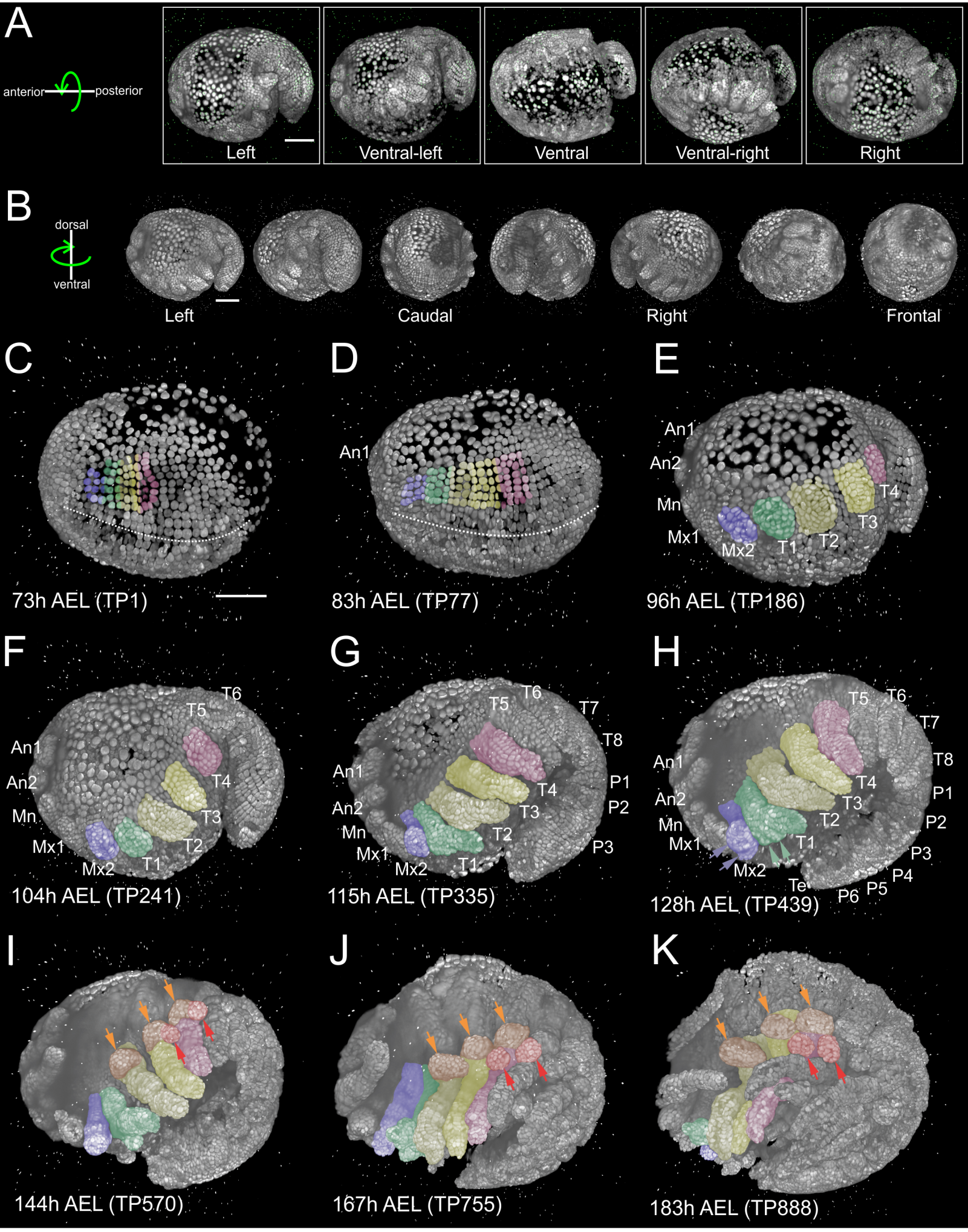
A
anterior
posterior
Left
Ventral-left
Ventral
Ventral-right
Right
B
dorsal
ventral
Left
Caudal
Right
Frontal
C
73h AEL (TP1)
D
An1
83h AEL (TP77)
E
An1
An2
Mn
Mx1
Mx2
T1
T2
T3
T4
96h AEL (TP186)
F
An1
An2
Mn
Mx1
Mx2
T1
T2
T3
T4
T5
T6
104h AEL (TP241)
G
An1
An2
Mn
Mx1
Mx2
T1
T2
T3
T4
T5
T6
T7
T8
P1
P2
P3
115h AEL (TP335)
H
An1
An2
Mn
Mx1
Mx2
Te
T1
T2
T3
T4
T5
T6
T7
T8
P1
P2
P3
P4
P5
P6
128h AEL (TP439)
I
144h AEL (TP570)
J
167h AEL (TP755)
K
183h AEL (TP888)

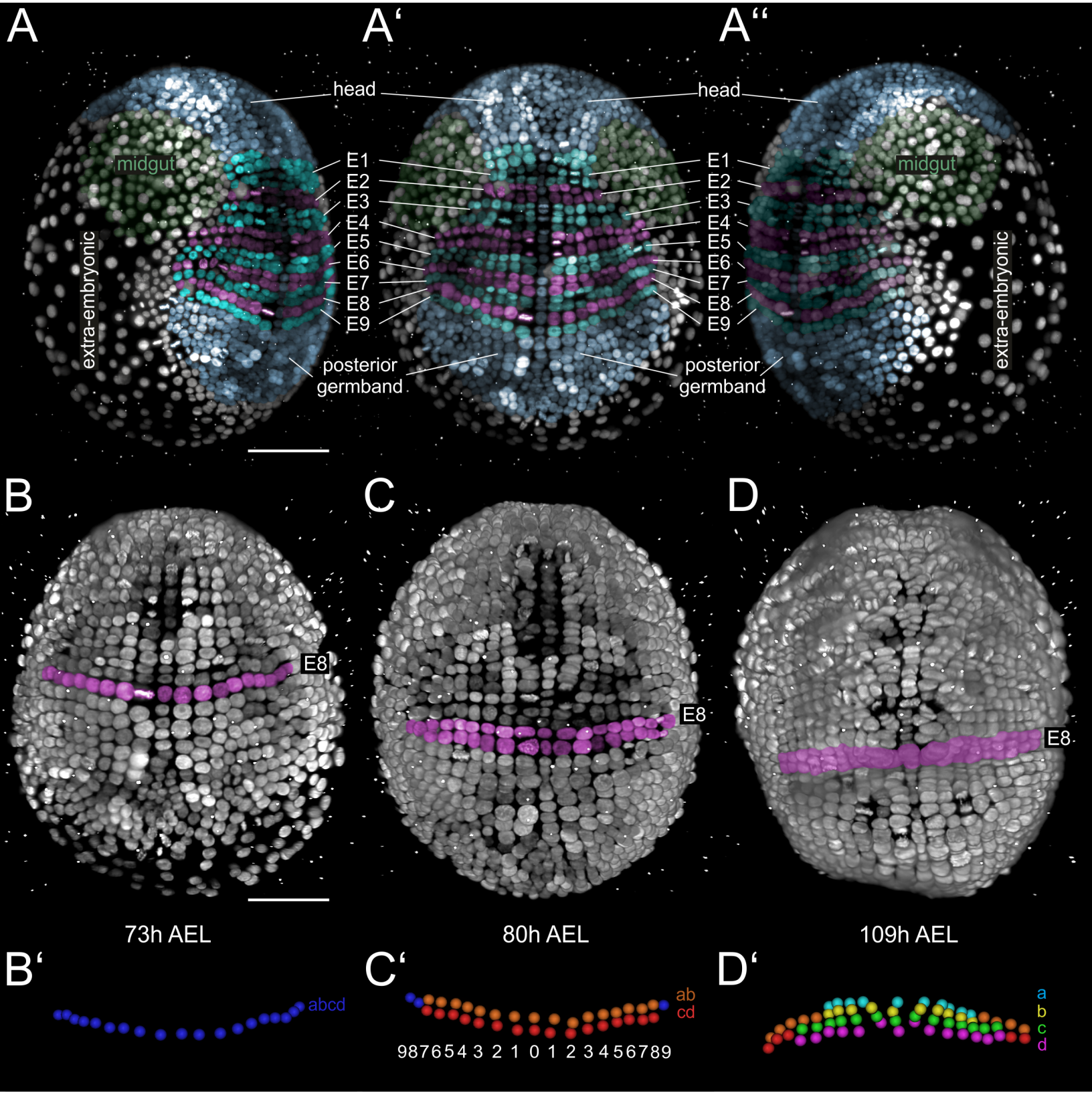
A
A‘
A“
head
head
midgut
midgut
E1
E2
E3
E4
E5
E6
E7
E8
E9
extra-embryonic
extra-embryonic
posterior germband
posterior germband
B
C
D
E8
E8
E8
73h AEL
80h AEL
109h AEL
B‘
C‘
D‘
abcd
ab
cd
9 8 7 6 5 4 3 2 1 0 1 2 3 4 5 6 7 8 9
a
b
c
d

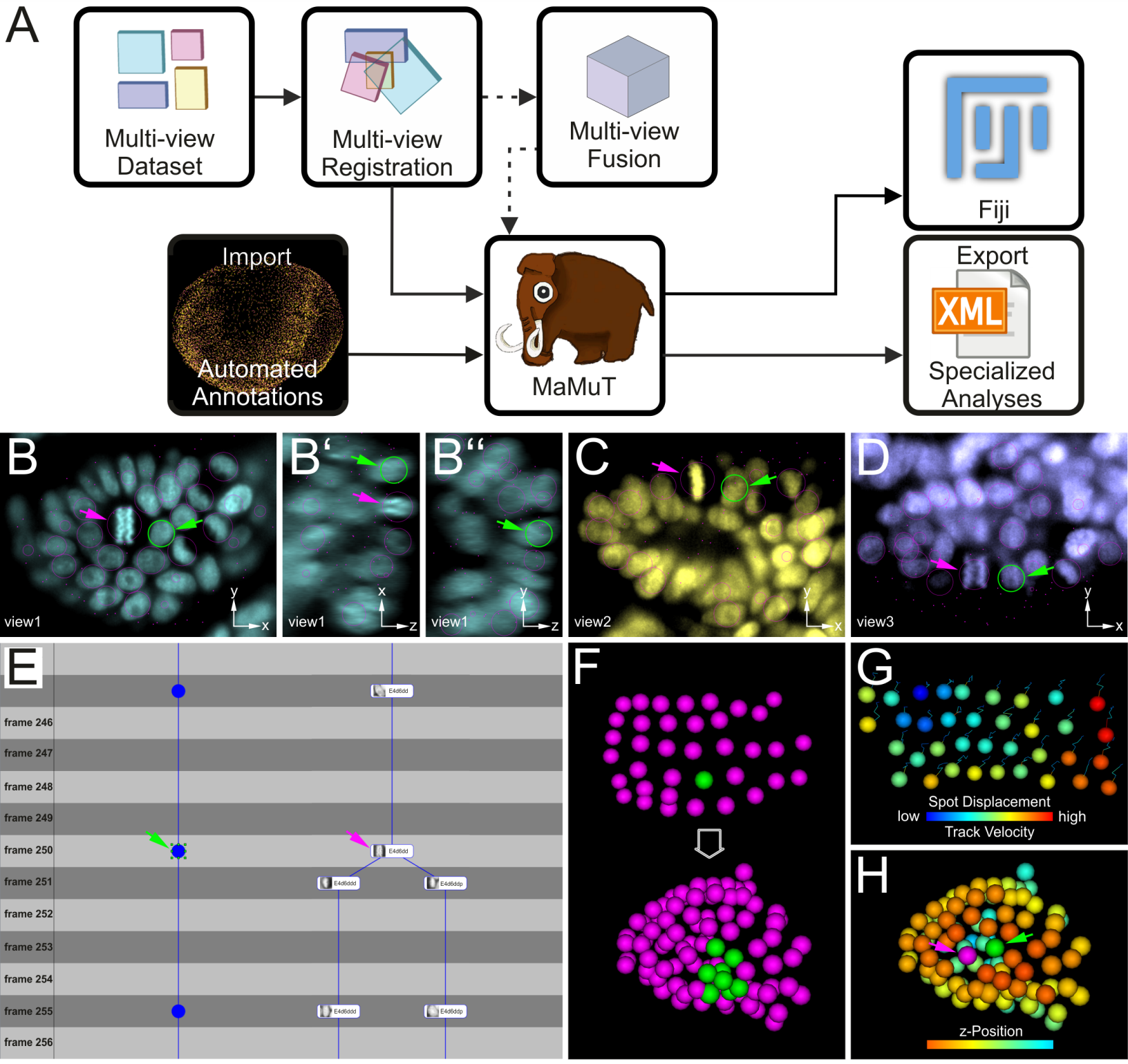
A
Multi-view Dataset
Multi-view Registration
Multi-view Fusion
Fiji
Import
Automated Annotations
MaMuT
Export
XML
Specialized Analyses
B
view1
B‘
view1
B“
view1
C
view2
D
view3
E
frame 246
frame 247
frame 248
frame 249
frame 250
frame 251
frame 252
frame 253
frame 254
frame 255
frame 256
F
G
Spot Displacement
low
high
Track Velocity
H
z-Position

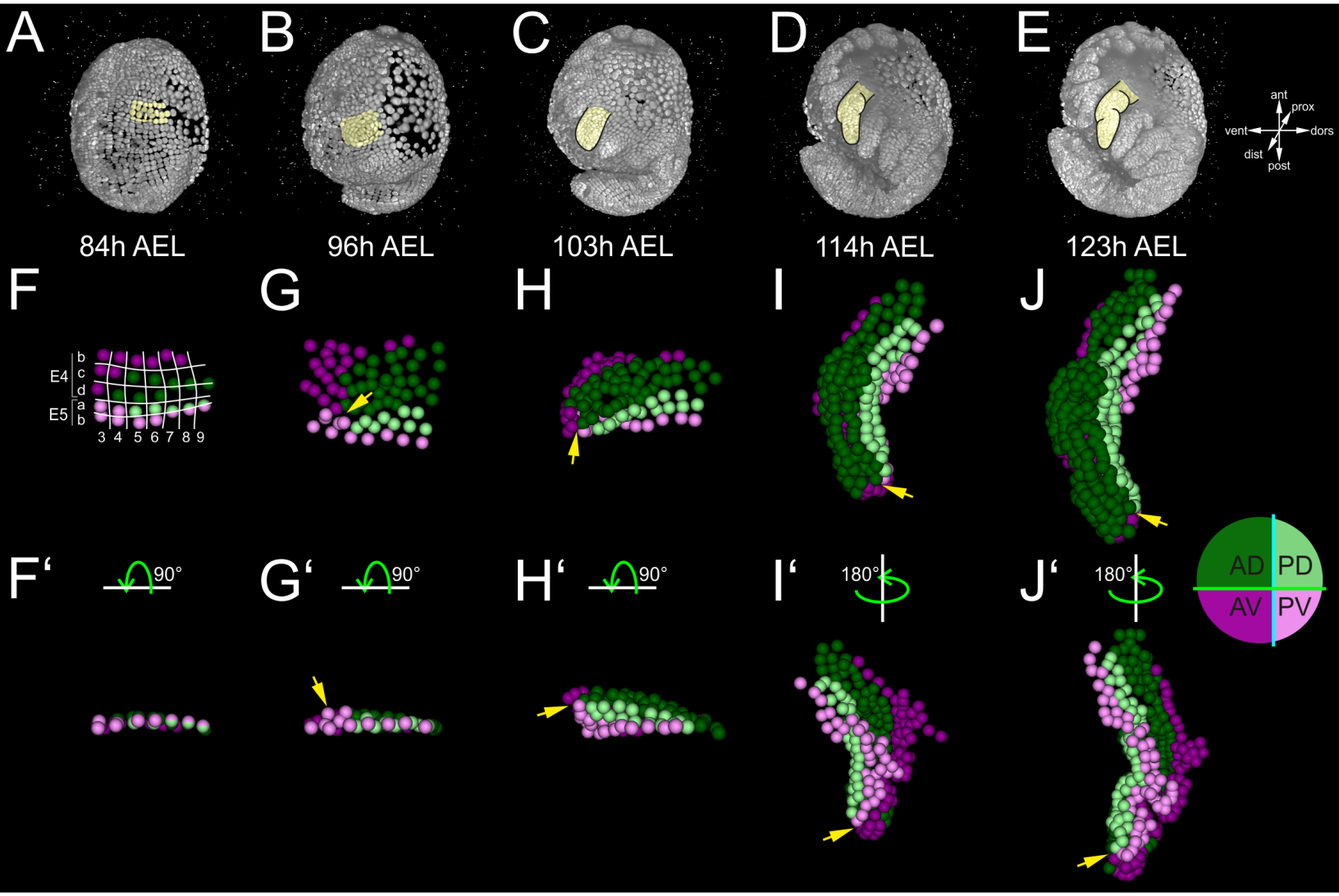
A
B
C
D
E
ant
prox
vent
dors
dist
post
84h AEL
96h AEL
103h AEL
114h AEL
123h AEL
F
G
H
I
J
E4
E5
b
c
d
a
b
3 4 5 6 7 8 9
F‘
G‘
H‘
I‘
J‘
90°
90°
90°
180°
180°
AD
PD
AV
PV

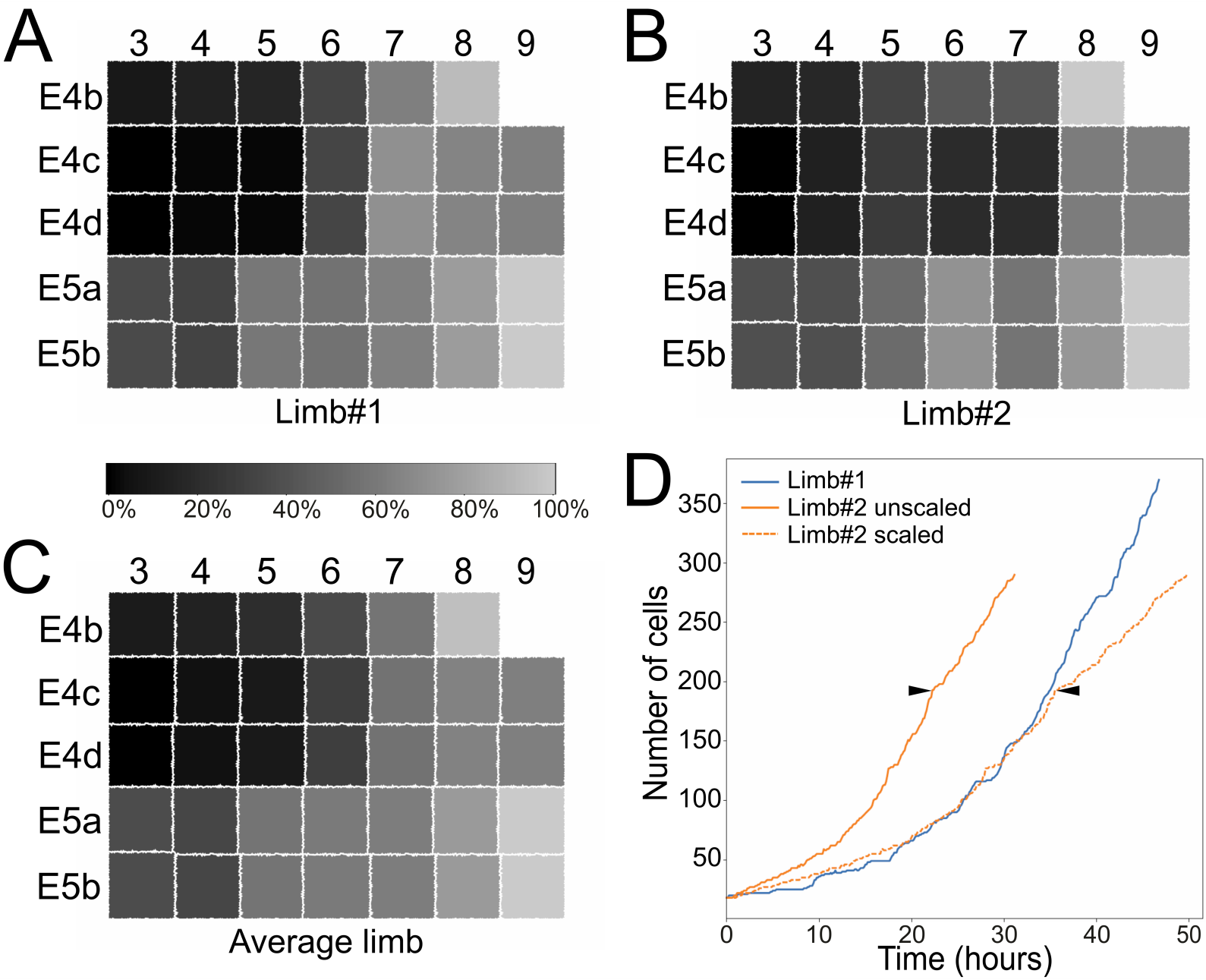
A
3 4 5 6 7 8 9
E4b
E4c
E4d
E5a
E5b
Limb#1
B
3 4 5 6 7 8 9
E4b
E4c
E4d
E5a
E5b
Limb#2
0% 20% 40% 60% 80% 100%
C
3 4 5 6 7 8 9
E4b
E4c
E4d
E5a
E5b
Average limb
D
Limb#1
Limb#2 unscaled
Limb#2 scaled
Number of cells
350
300
250
200
150
100
50
0 10 20 30 40 50
Time (hours)

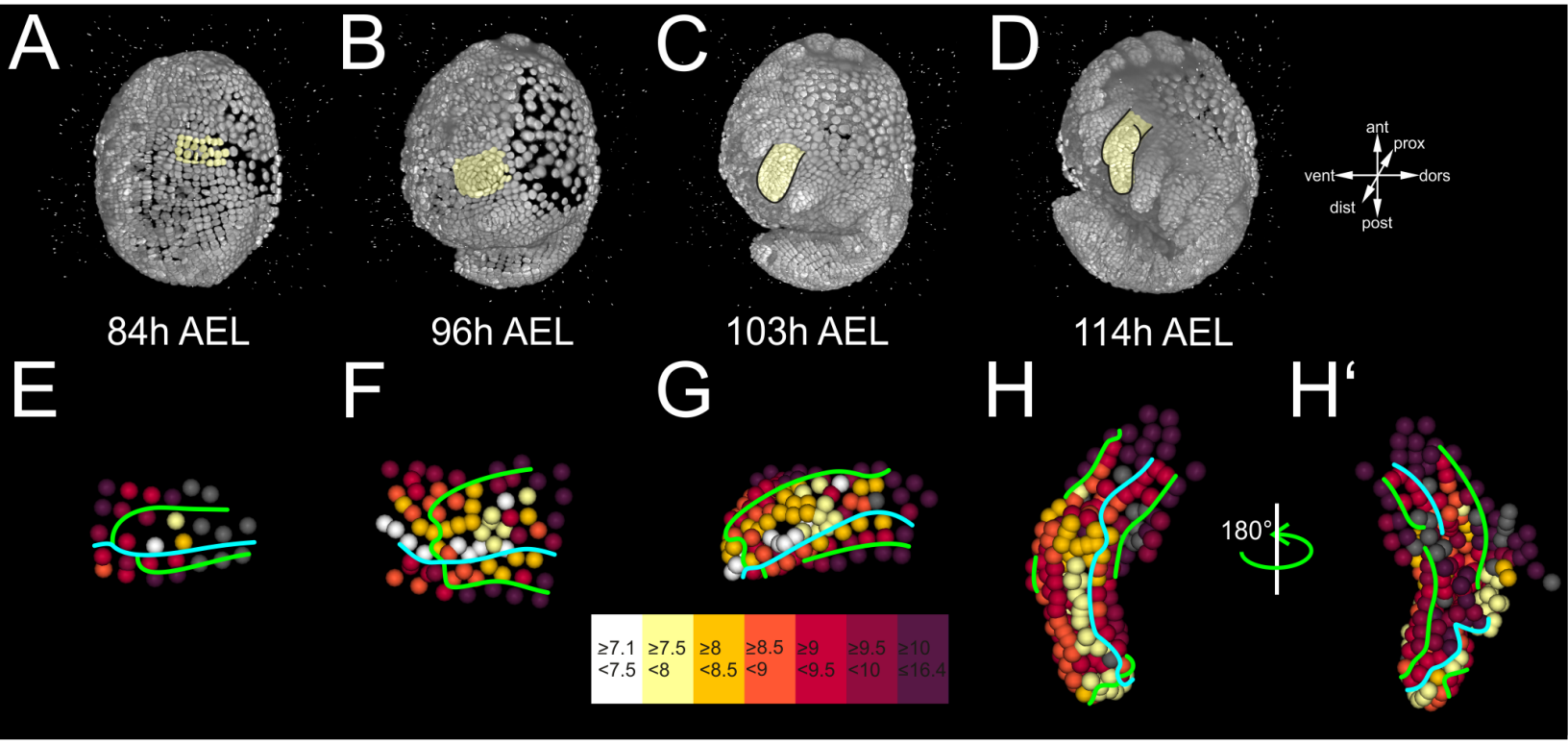
A
B
C
D
ant
prox
vent
dors
dist
post
84h AEL
96h AEL
103h AEL
114h AEL
E
F
G
H
H‘
≥7.1 <7.5
≥7.5 <8
≥8 <8.5
≥8.5 <9
≥9 <9.5
≥9.5 <10
≥10 ≤16.4
180°

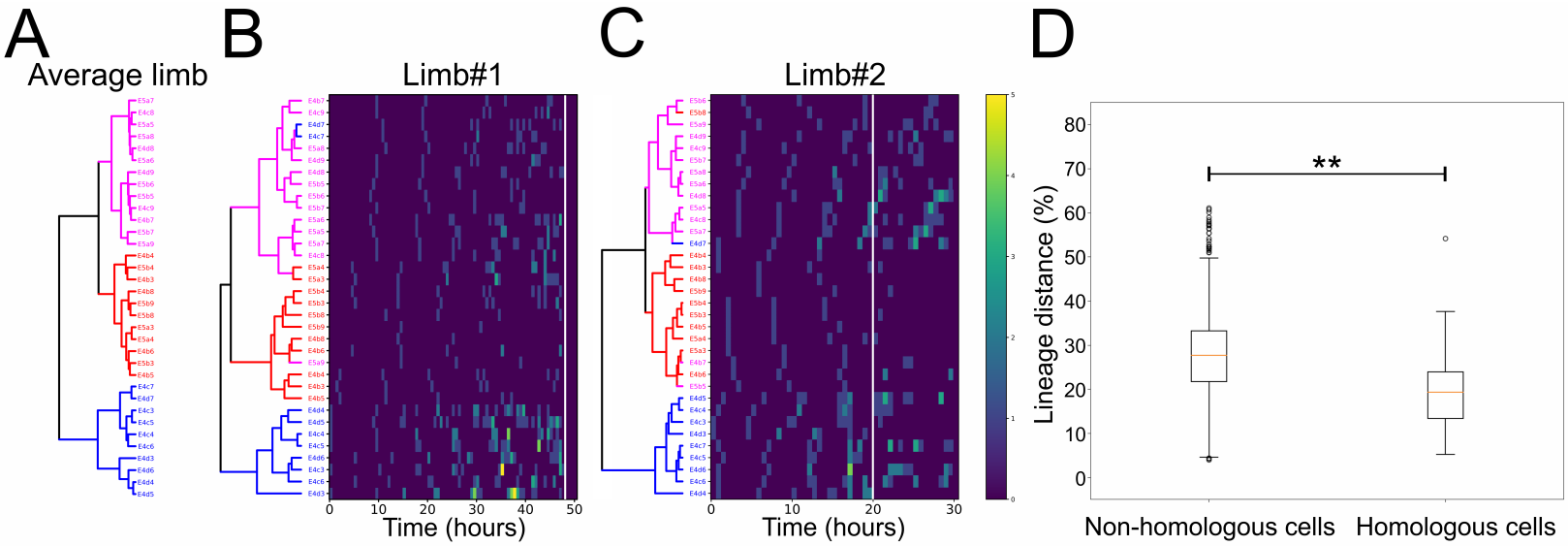
A
Average limb
B
Limb#1
Time (hours)
C
Limb#2
Time (hours)
D
Lineage distance (%)
**
Non-homologous cells
Homologous cells

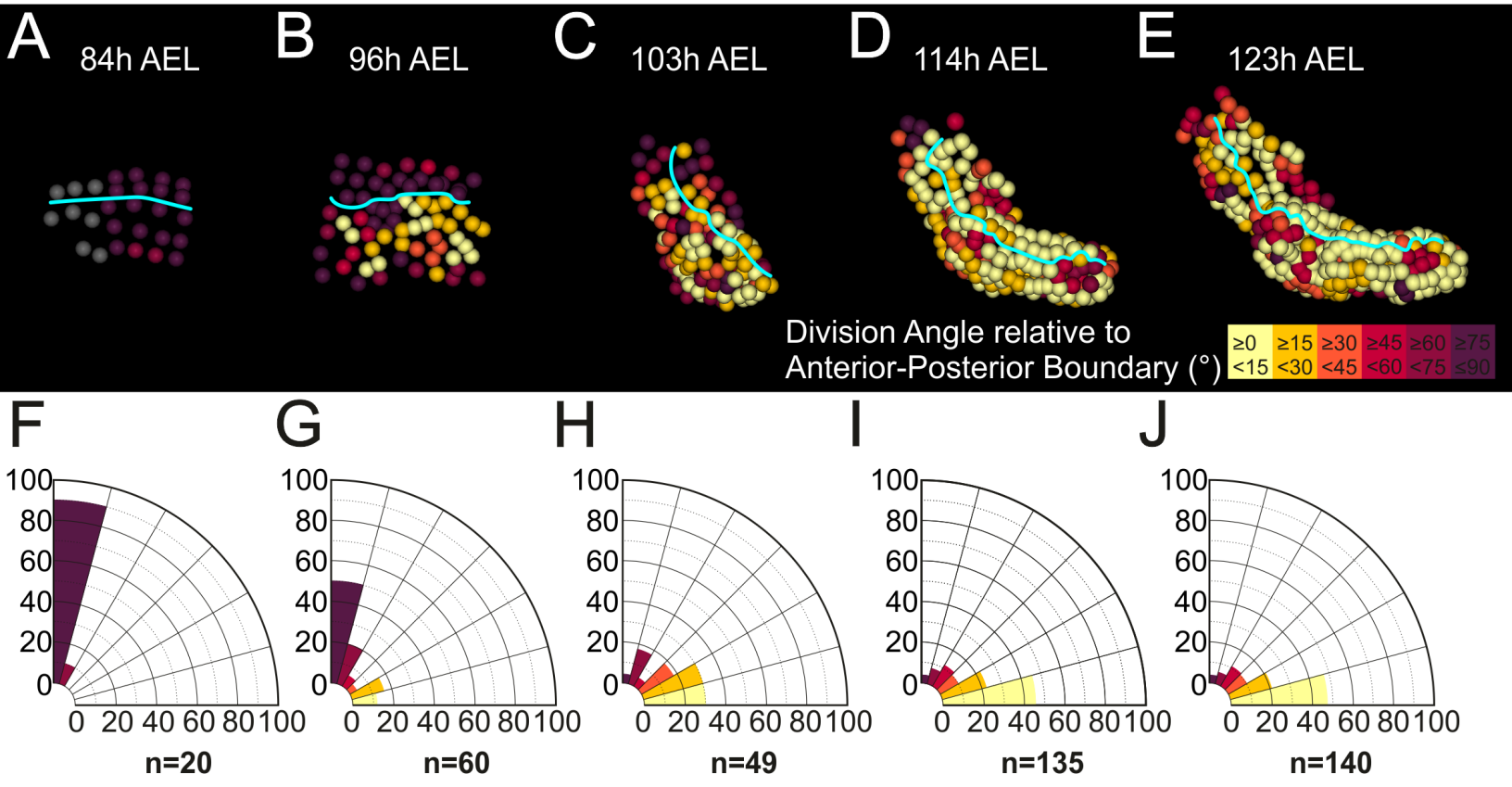
A
84h AEL
B
96h AEL
C
103h AEL
D
114h AEL
E
123h AEL
Division Angle relative to
Anterior-Posterior Boundary (°)
≥0 <15
≥15 <30
≥30 <45
≥45 <60
≥60 <75
≥75 ≤90

F
G
H
I
J
100
80
60
40
20
0
0 20 40 60 80 100
n=20
n=60
n=49
n=135
n=140

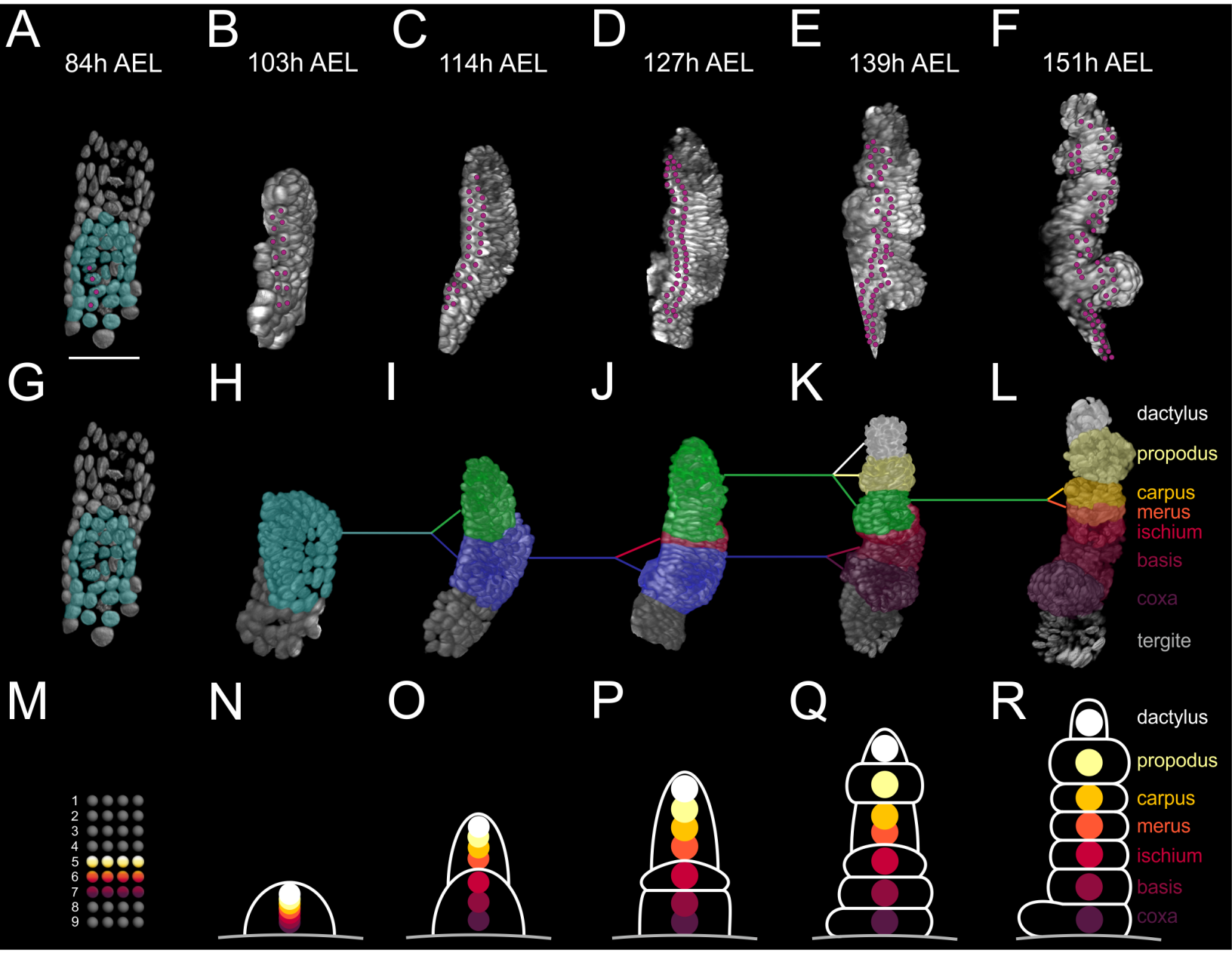
A
84h AEL
B
103h AEL
C
114h AEL
D
127h AEL
E
139h AEL
F
151h AEL
G
H
I
J
K
L
dactylus
propodus
carpus
merus
ischium
basis
coxa
tergite
M
1
2
3
4
5
6
7
8
9
N
O
P
Q
R
dactylus
propodus
carpus
merus
ischium
basis
coxa

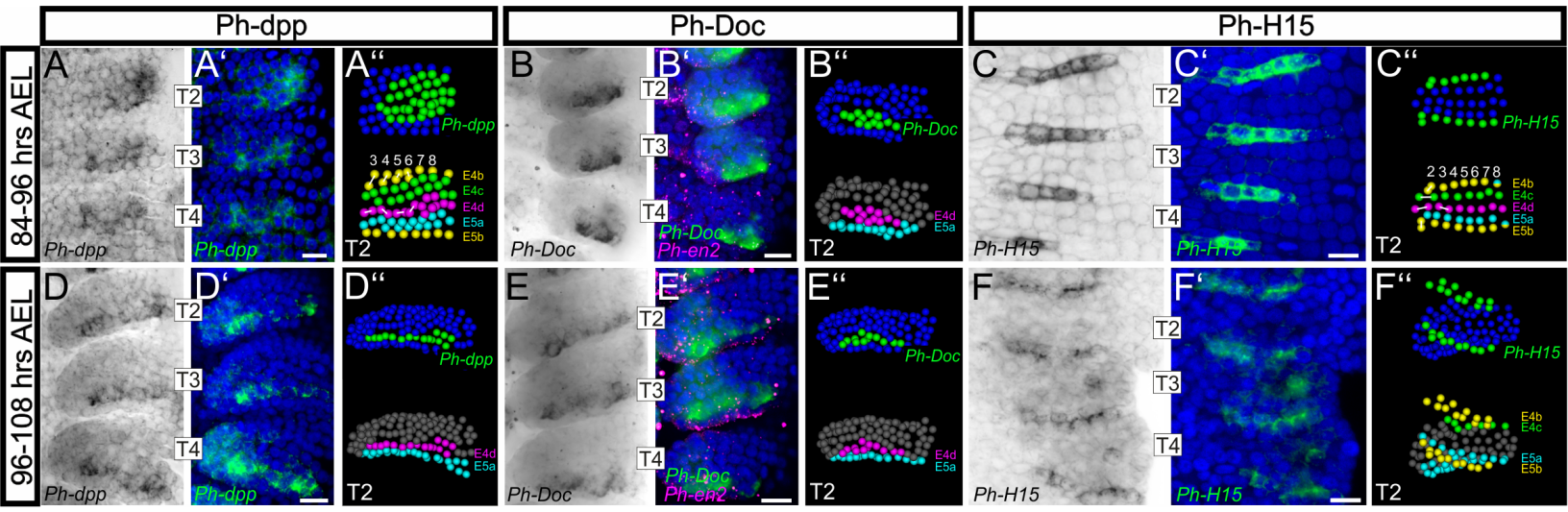
Ph-dpp
Ph-Doc
Ph-H15
84-96 hrs AEL
96-108 hrs AEL
A
A'
A''
B
B'
B''
C
C'
C''
D
D'
D''
E
E'
E''
F
F'
F''
T2
T3
T4
Ph-dpp
Ph-Doc
Ph-en2
Ph-H15
3 4 5 6 7 8
2 3 4 5 6 7 8
E4b
E4c
E4d
E5a
E5b

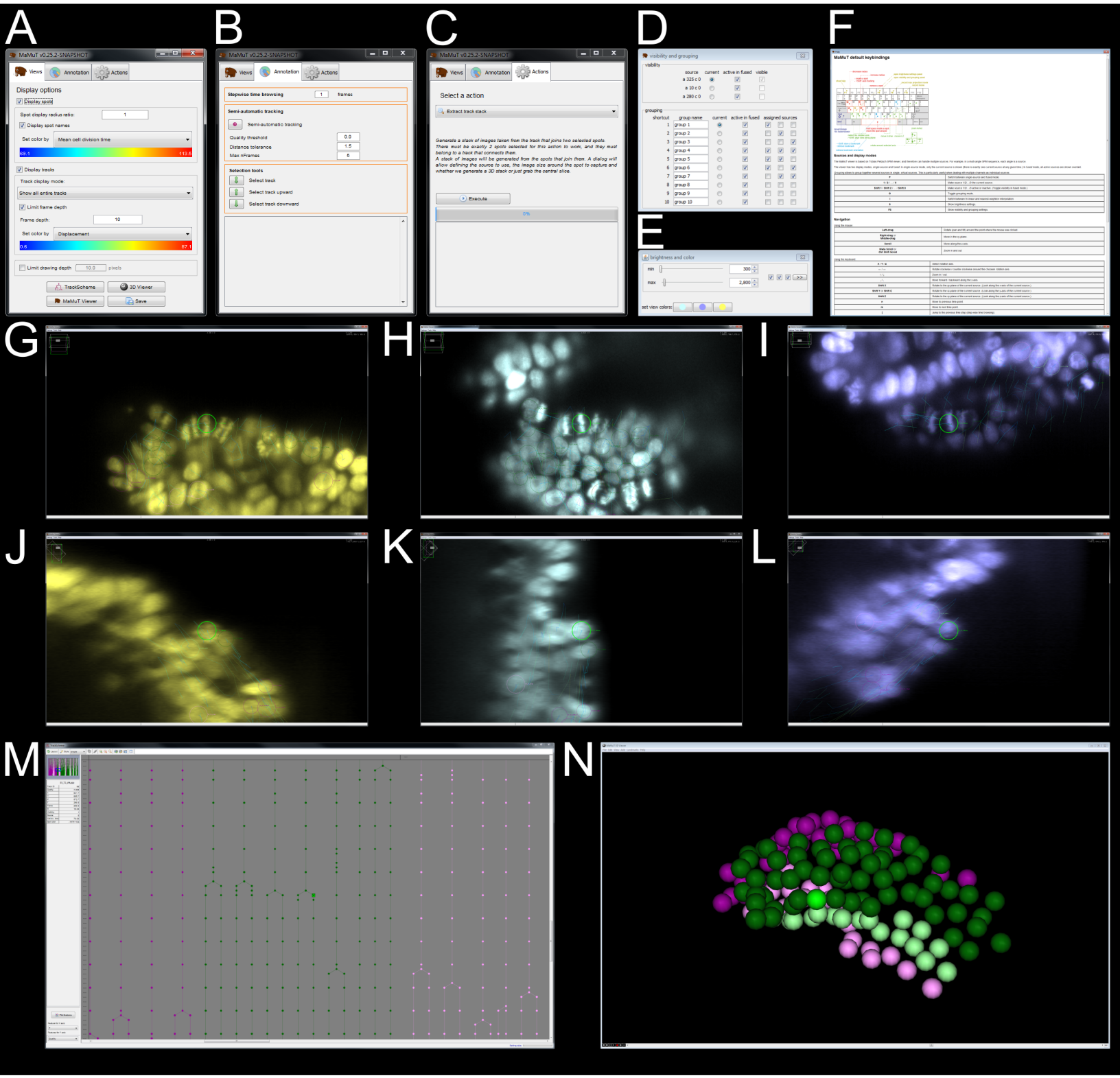
A
MaMuT v0.25.2-SNAPSHOT
Views
Annotation
Actions
Display options
Display spots
Spot display radius ratio:
Display spot names
Set color by
Mean cell division time
Display tracks
Track display mode:
Show all entire tracks
Limit frame depth
Frame depth:
Displacement
Limit drawing depth
pixels
TrackScheme
3D Viewer
MaMuT Viewer
Save
B
Stepwise time browsing
frames
Semi-automatic tracking
Quality threshold
Distance tolerance
Max nFrames
Selection tools
Select track
Select track upward
Select track downward
C
Select a action
Extract track stack
Generate a stack of images taken from the track that joins two selected spots.
There must be exactly 2 spots selected for this action to work, and they must belong to a track that connects them.
A stack of images will be generated from the spots that join them. A dialog will allow defining the source to use, the image size around the spot to capture and whether we generate a 3D stack or just grab the central slice.
Execute
D
visibility and grouping
visibility
source
current
active in fused
visible
grouping
shortcut
group name
assigned sources
E
brightness and color
min
max
set view colors:
F
MaMuT default keybindings
G
H
I
J
K
L
M
N

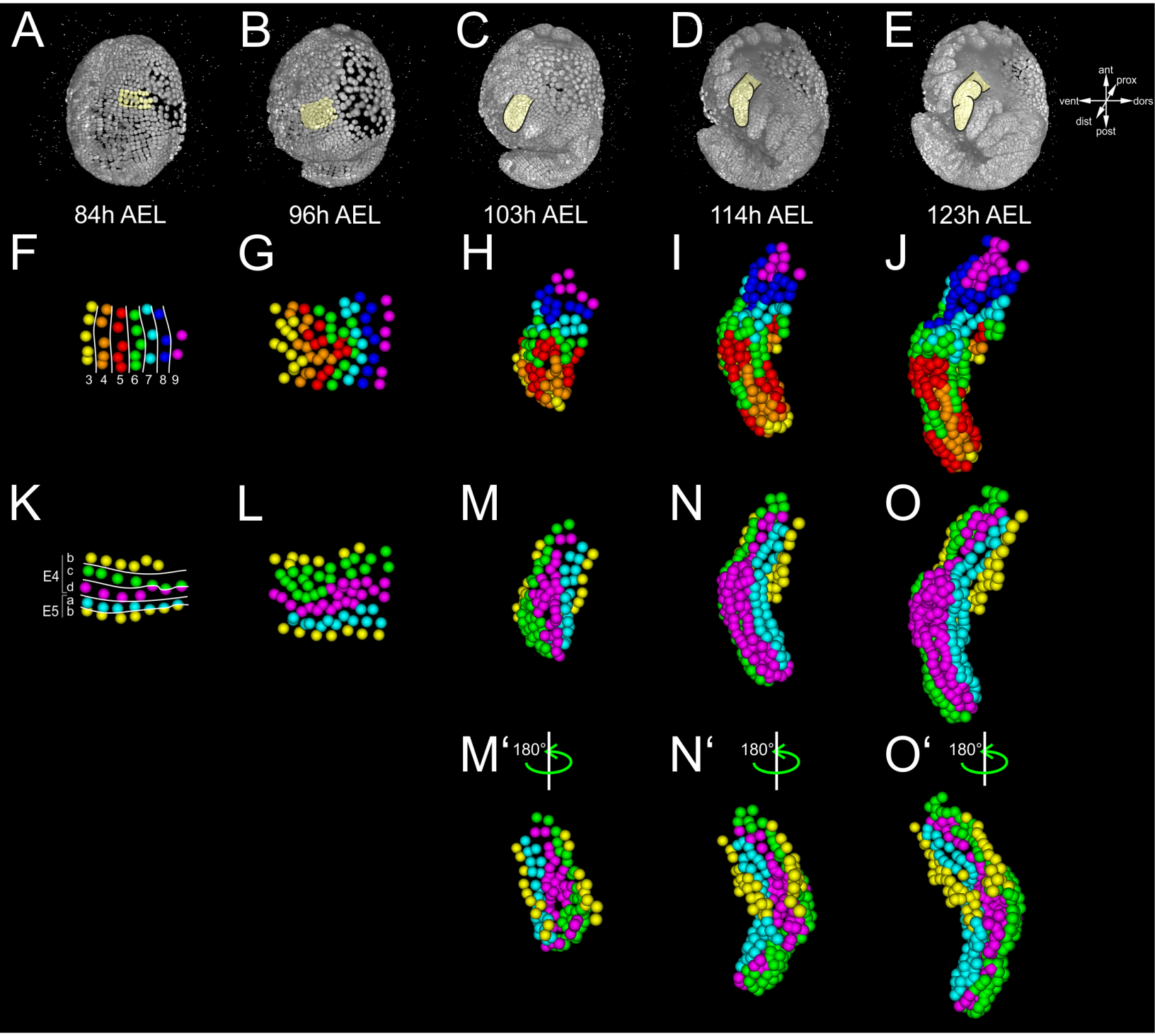
A
B
C
D
E
ant
prox
vent
dors
dist
post
84h AEL
96h AEL
103h AEL
114h AEL
123h AEL
F
G
H
I
J
3 4 5 6 7 8 9
K
L
M
N
O
E4
E5
b
c
d
a
b
M‘
N‘
O‘
180°
180°
180°

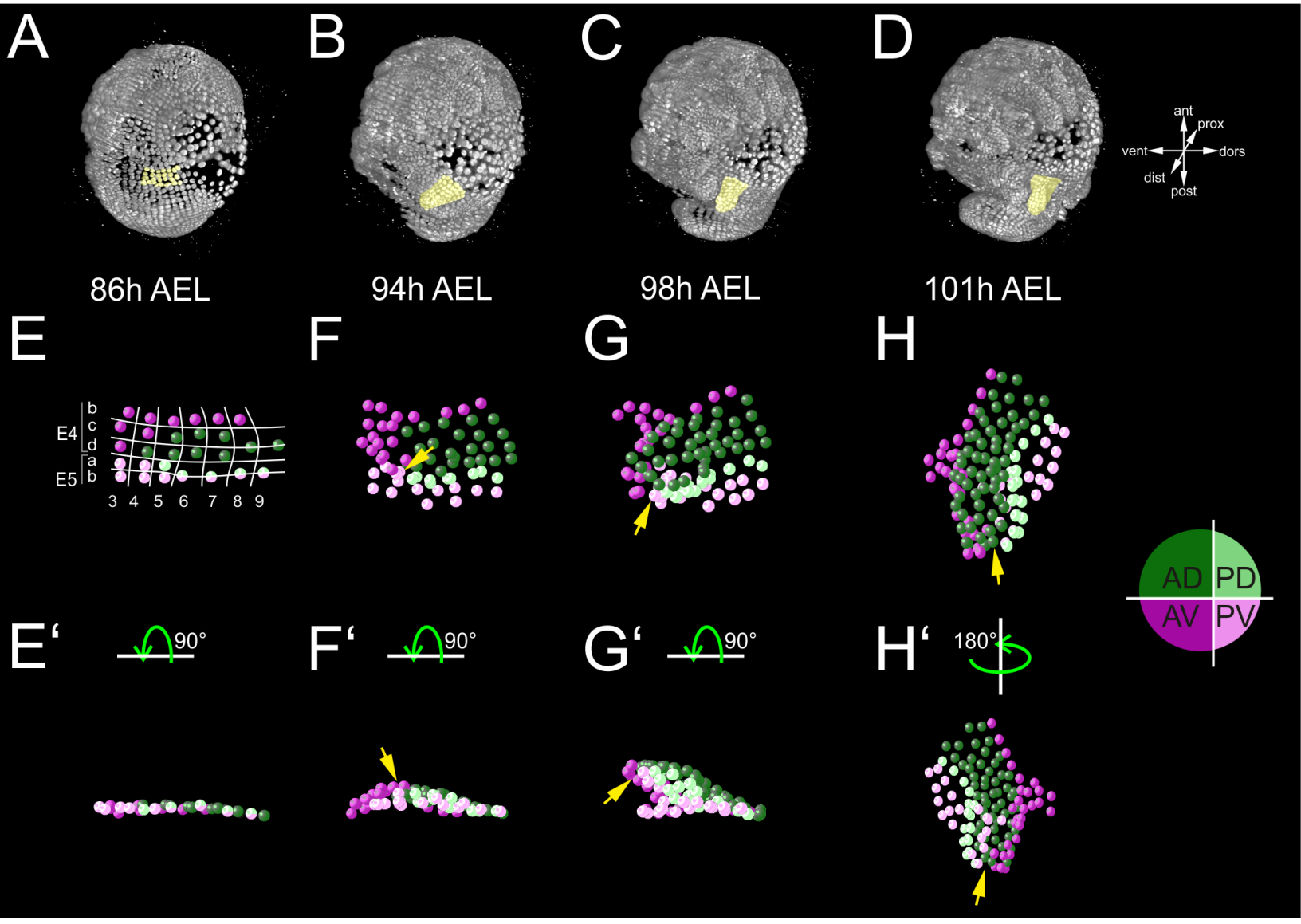
A
B
C
D
ant
prox
vent
dors
dist
post
86h AEL
94h AEL
98h AEL
101h AEL
E
F
G
H
E4
b
c
d
E5
a
b
3 4 5 6 7 8 9
AD
PD
AV
PV
E‘
F‘
G‘
H‘
90°
90°
90°
180°

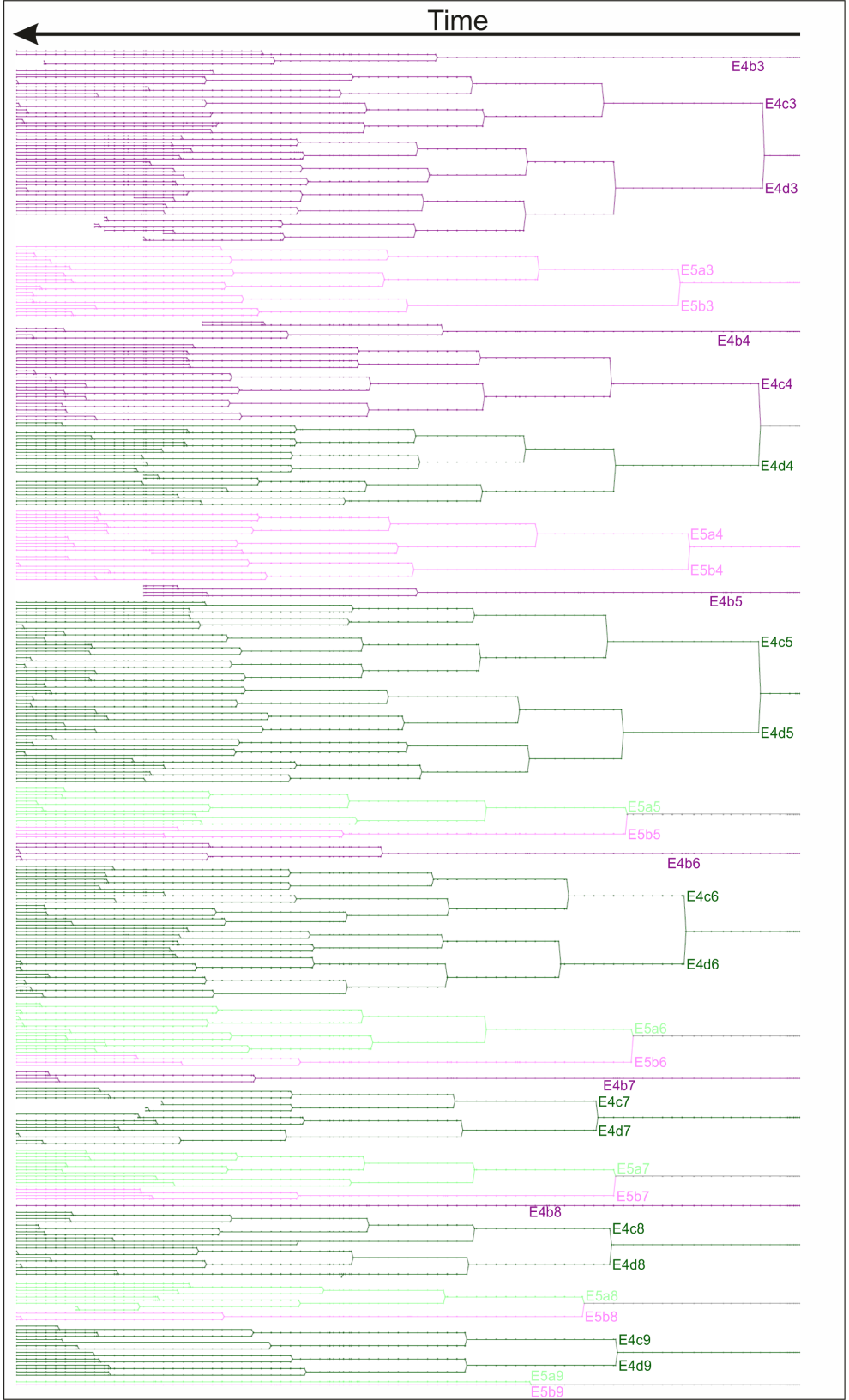
Time
E4b3
E4c3
E4d3
E5a3
E5b3
E4b4
E4c4
E4d4
E5a4
E5b4
E4b5
E4c5
E4d5
E5a5
E5b5
E4b6
E4c6
E4d6
E5a6
E5b6
E4b7
E4c7
E4d7
E5a7
E5b7
E4b8
E4c8
E4d8
E5a8
E5b8
E4c9
E4d9
E5a9
E5b9

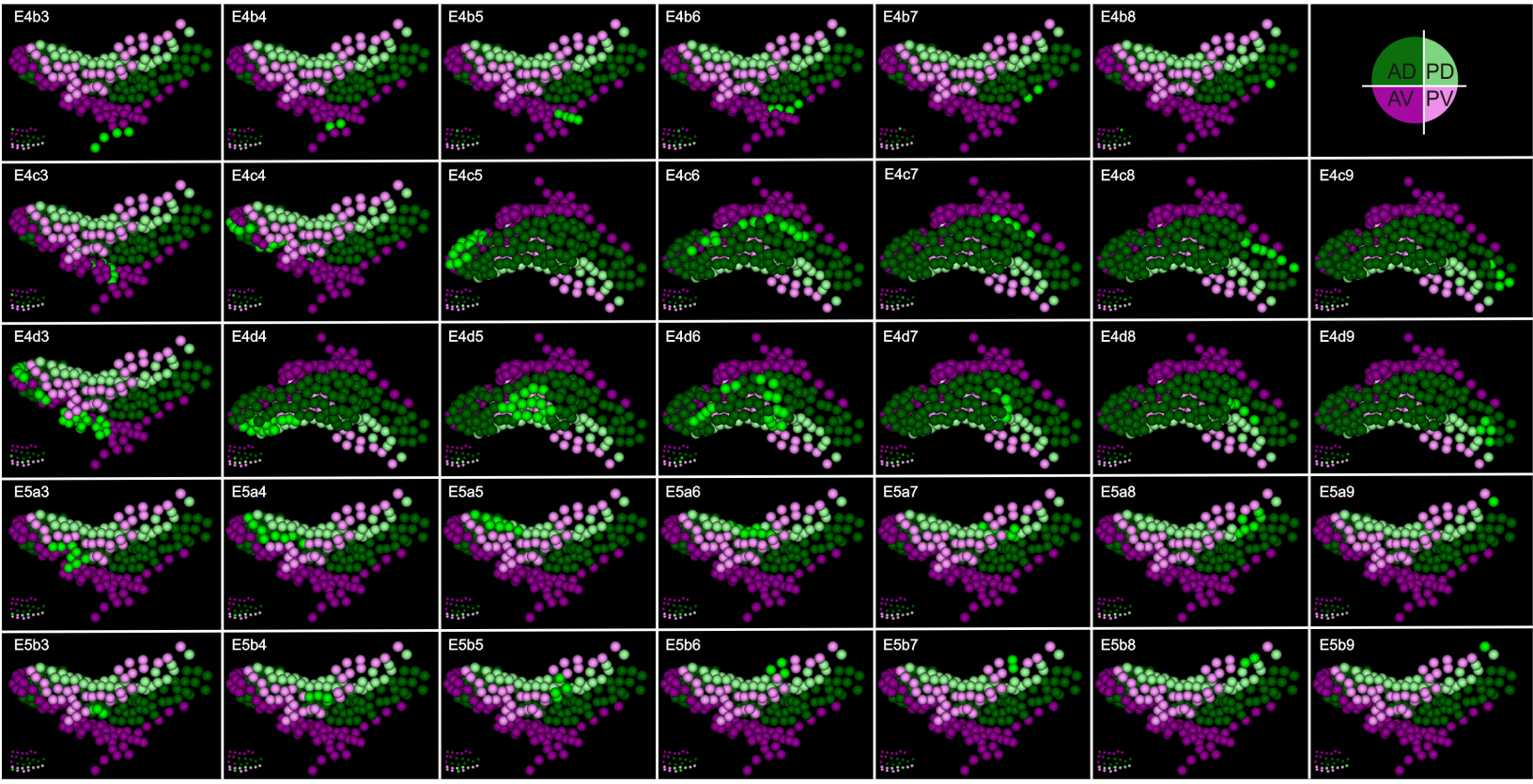
E4b3
E4b4
E4b5
E4b6
E4b7
E4b8
AD
PD
AV
PV
E4c3
E4c4
E4c5
E4c6
E4c7
E4c8
E4c9
E4d3
E4d4
E4d5
E4d6
E4d7
E4d8
E4d9
E5a3
E5a4
E5a5
E5a6
E5a7
E5a8
E5a9
E5b3
E5b4
E5b5
E5b6
E5b7
E5b8
E5b9

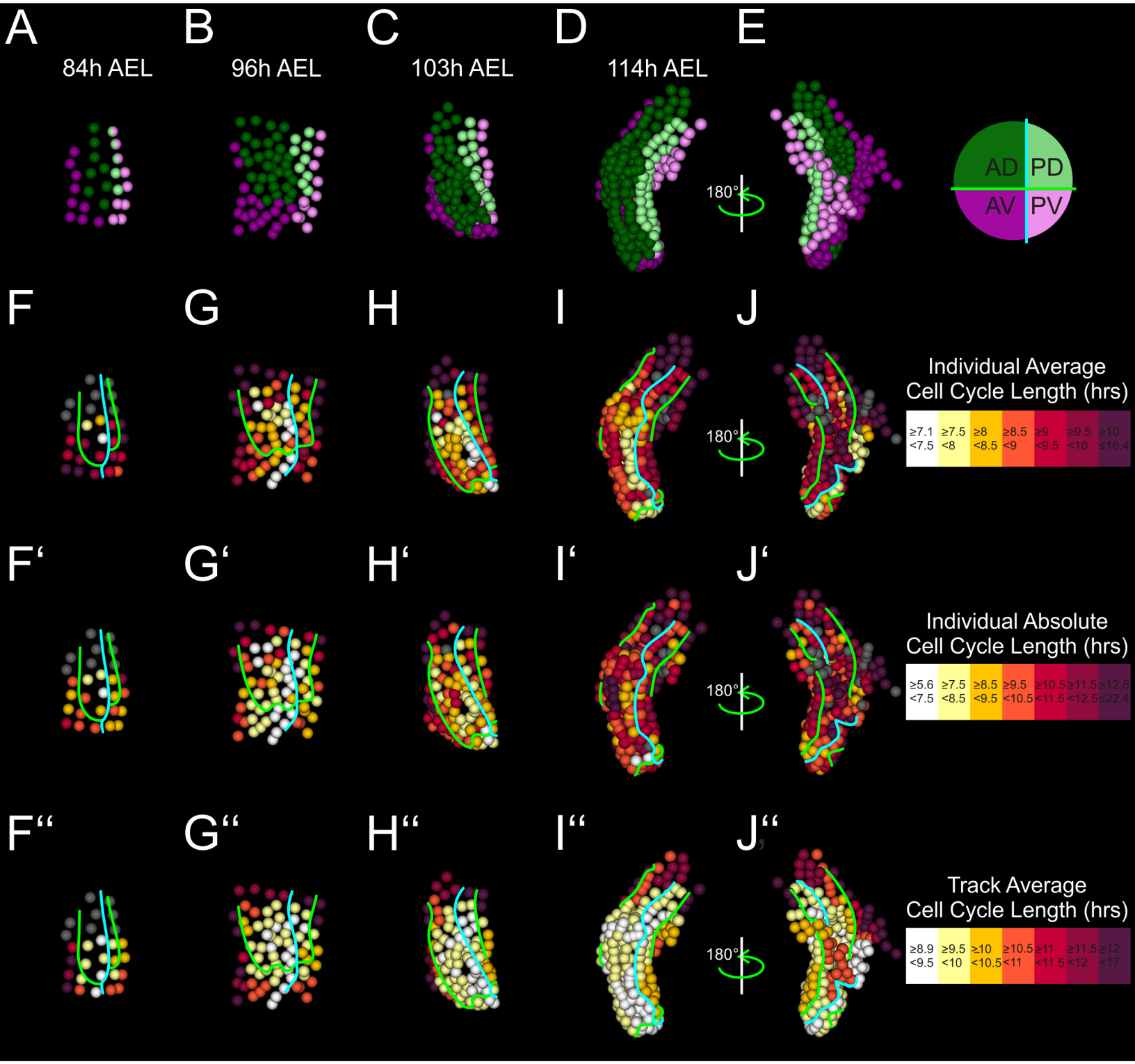
A
84h AEL
B
96h AEL
C
103h AEL
D
114h AEL
E
180°
AD
PD
AV
PV
F
G
H
I
J
180°
Individual Average
Cell Cycle Length (hrs)
≥7.1 <7.5
≥7.5 <8
≥8 <8.5
≥8.5 <9
≥9 <9.5
≥9.5 <10
≥10 ≤16.4
F‘
G‘
H‘
I‘
J‘
180°
Individual Absolute
Cell Cycle Length (hrs)
≥5.6 <7.5
≥7.5 <8.5
≥8.5 <9.5
≥9.5 <10.5
≥10.5 <11.5
≥11.5 <12.5
≥12.5 ≤22.4
F“
G“
H“
I“
J“
180°
Track Average
Cell Cycle Length (hrs)
≥8.9 <9.5
≥9.5 <10
≥10 <10.5
≥10.5 <11
≥11 <11.5
≥11.5 <12
≥12 <17

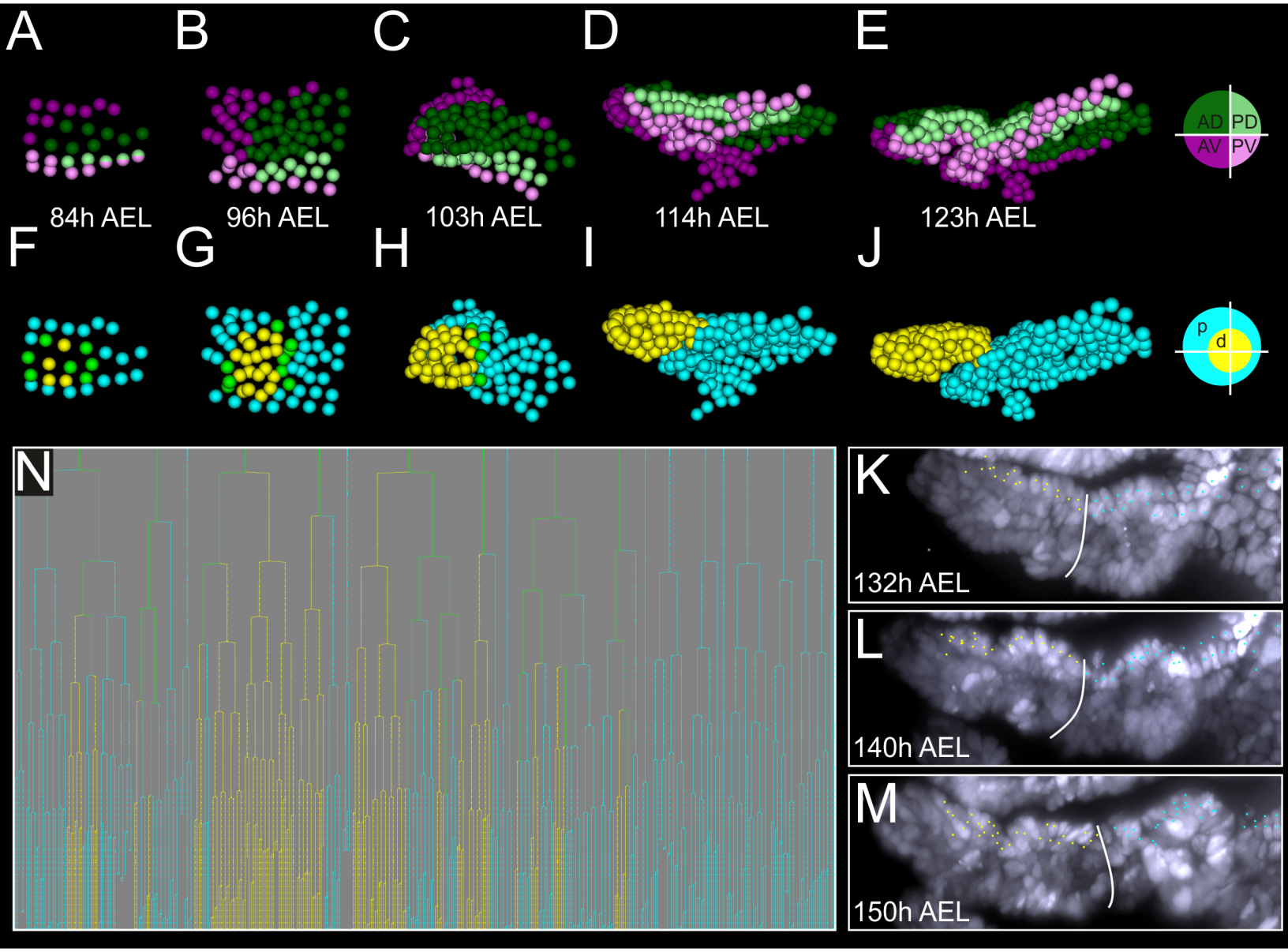
A
B
C
D
E
84h AEL
96h AEL
103h AEL
114h AEL
123h AEL
AD
PD
AV
PV
F
G
H
I
J
p
d
N
K
132h AEL
L
140h AEL
M
150h AEL

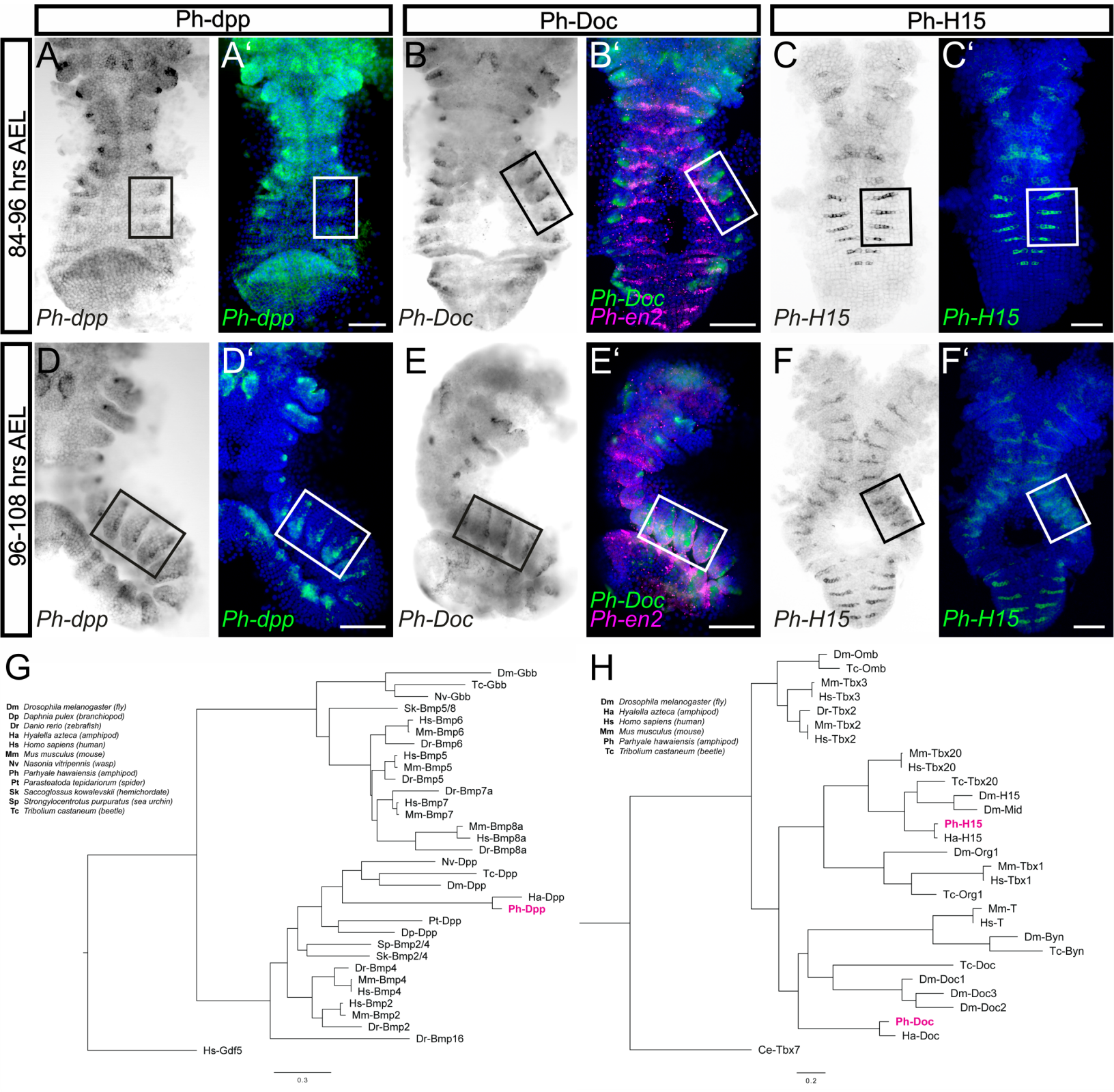
Ph-dpp
Ph-Doc
Ph-H15
84-96 hrs AEL
96-108 hrs AEL
A
A'
B
B'
C
C'
D
D'
E
E'
F
F'
Ph-dpp
Ph-Doc
Ph-en2
Ph-H15

G
Dm Drosophila melanogaster (fly)
Dp Daphnia pulex (branchiopod)
Dr Danio rerio (zebrafish)
Ha Hyalella azteca (amphipod)
Hs Homo sapiens (human)
Mm Mus musculus (mouse)
Nv Nasonia vitripennis (wasp)
Ph Parhyale hawaiensis (amphipod)
Pt Parasteatoda tepidariorum (spider)
Sk Saccoglossus kowalevskii (hemichordate)
Sp Strongylocentrotus purpuratus (sea urchin)
Tc Tribolium castaneum (beetle)
Dm-Gbb
Tc-Gbb
Nv-Gbb
Sk-Bmp5/8
Hs-Bmp6
Mm-Bmp6
Dr-Bmp6
Hs-Bmp5
Mm-Bmp5
Dr-Bmp5
Dr-Bmp7a
Hs-Bmp7
Mm-Bmp7
Mm-Bmp8a
Hs-Bmp8a
Dr-Bmp8a
Nv-Dpp
Tc-Dpp
Dm-Dpp
Ha-Dpp
Ph-Dpp
Pt-Dpp
Dp-Dpp
Sp-Bmp2/4
Sk-Bmp2/4
Dr-Bmp4
Mm-Bmp4
Hs-Bmp4
Hs-Bmp2
Mm-Bmp2
Dr-Bmp2
Dr-Bmp16
Hs-Gdf5
0.3

H
Dm Drosophila melanogaster (fly)
Ha Hyalella azteca (amphipod)
Hs Homo sapiens (human)
Mm Mus musculus (mouse)
Ph Parhyale hawaiensis (amphipod)
Tc Tribolium castaneum (beetle)
Dm-Omb
Tc-Omb
Mm-Tbx3
Hs-Tbx3
Dr-Tbx2
Mm-Tbx2
Hs-Tbx2
Mm-Tbx20
Hs-Tbx20
Tc-Tbx20
Dm-H15
Dm-Mid
Ph-H15
Ha-H15
Dm-Org1
Mm-Tbx1
Hs-Tbx1
Tc-Org1
Mm-T
Hs-T
Dm-Byn
Tc-Byn
Tc-Doc
Dm-Doc1
Dm-Doc3
Dm-Doc2
Ph-Doc
Ha-Doc
Ce-Tbx7
0.2